TESLA Report 2003-10

Studies of Electromagnetic Cascade Showers Development in the TESLA Main Linac Initiated by Electron Field Emission in RF Cavities

V. Balandin, R. Brinkmann, K. Flöttmann, and N. Golubeva
Deutsches Elektronen-Synchrotron DESY, Hamburg

Contents

1 Introduction

Parasitic electrons can be produced inside an accelerator structure by a variety of ways. For example, by ionizing processes in the residual gas of the imperfect vacuum, by quantum-mechanical tunneling of electrons from cold metal into vacuum in the presence of sufficiently high surface electric fields (field emission), by excitations of electrons in the vacuum chamber walls after a primary electron impact (secondary electron emission), and etc. The need to understand and control the influence of these electrons on the accelerator performance has become increasingly important due to the prospects of using high-gradient structures in future linear colliders, because parasitic particles can absorb significant energy from their interaction with the cavity field and as a result create dark current, produce radiation, and even lead to rf breakdown.

Significant progress achieved in the last decades in fabrication and testing of high-gradient accelerating structures was accompanied by extensive theoretical and numerical studies stimulated by the desire to systematize and explain the large amount of accumulated experimental data and understand cavity gradient limiting mechanisms (see, for example, [2] - [8]).

As concerning dynamics, the majority of available papers is also connected with the study of the behaviour of the parasitic particles within a single accelerating structure (see, for example, [9] - [17]), and most of these papers are important multipactor studies. The possibility, that a certain amount of parasitic particles will be captured by the RF-field and then this captured current will build up along the accelerator, is not studied in so many details yet as local, single accelerating unit problems. The typical point of view on this subject, supported by a few papers (see, for example, [18] and [19]), is that most of these captured particles will be over-focused and eliminated by the quadrupole array. These numerical investigations of the problem follow approximately the same calculation scheme. At first the distribution of electrons at the exit of one accelerating unit (cavity or chain of cavities) is obtained. Usually, this step is done quite accurately and include a realistic geometry of the cavity walls, electromagnetic fields coming from some field solver, field emission and, possibly, secondary electron emission models. Then the simulation is continued using, for example, some standard tracking code or specially written thin lens tracking procedure. In both cases this second step uses essentially simplified wall geometries and accelerating field models, and do not include particle multiplication effects similar, for

example, to secondary electron emission. So after such studies one can speak correctly about the elimination of particles coming out of the first accelerating unit , and can in general not conclude that current created by them will be eliminated too, because, when impacting the surface of the cavity, a primary particle might create some number of secondaries, depending on the impact energy and material.

In the Main Linac of the TESLA Linear Collider [1] field emitted particles can be accelerated to hundreds of MeV before being kicked out by quadrupoles and thus will originate electromagnetic cascade showers in the accelerator materials. Some of the shower secondaries can return back into the vacuum and can be re-accelerated by the cavity RF-field, and will then be again kicked out by quadrupoles, and so, generally speaking, we can end up with an avalanche of fastly increasing dark current. The question, if this multiplication mechanism can be a real problem for the TESLA Main Linac, is the main subject of this paper, and, in order to see this point more clearly, none of the other possible particle multiplication processes will be included in our simulations.

2 Simulation Procedure and Code Design

The process of particle transport in our computer code DUST (DUnkel STrom, in German) is organized in such a way that it naturally breaks down into two parts, Monte Carlo simulation of the electromagnetic shower development when a particle impacts the inner vacuum surface of the accelerator, and particle dynamics in an electromagnetic field inside the accelerator vacuum. As usual, the accelerator to be studied is described as a sequence of physical elements. The user specifies the element geometry, materials and electromagnetic fields. And although we have not implemented something similar to the MAD [20] lattice description language yet, to simplify the accelerator description, elements in our program can be grouped into different modules, from modules one constructs cells, and a sequence of cells forms the linac.

2.1 Particle Transport in Nonvacuum Media

When an energetic primary particle incidents on a mass of material of sufficient thickness a cascade of particles and electromagnetic radiation of

great complexity results, and the most practical way to obtain the characteristics of this cascade, the distribution and parameters of secondary particles, especially for complicated material geometries, is through Monte Carlo simulations. Even though a code for the transport of high energy particles (in GeV range) can be developed without too great complications (see, for example, [21], [22]), the accurate simulation of the low energy particles is a very demanding effort. So, it is obvious, that it is better to use a thoroughly tested, standard programme, based on an extensive and regularly updated cross-sections data base. We have chosen the EGS4 (Electron-Gamma-Shower) [23] software package for fast Monte Carlo simulations of the coupled electron-photon transport, which can accurately simulate particles interactions spanning the $10\,keV - 1\,TeV$ energy range.

2.1.1 Interface with EGS4

The user interface with the EGS4 system is simple and very flexible. Following well-specified rules [23] and viewing EGS4 as a set of subroutines, we have successfully incorporated this program into our computer code DUST. Because the EGS4 design allows itself to concern only with the problem of particle transport in an infinite media, it was necessary to write subroutines which will compute the distance along a particle motion direction at which a surface describing the material geometry is intersected. To have both, a fast and robust, distance to boundary calculation algorithm, the material geometry in the current version of our code is restricted to be an axisymmetrical combination of piecewise conical surfaces, for which an analytical solution of the problem is available.

2.1.2 Updating Time Variable of the Particle

We have extended the EGS4 standard set of variables for the particle description to include such quantities as laboratory time and particle generation number. The latter will be discussed below in this paper and for updating the particle time coordinate the following formula is used

$$\Delta t \;=\; \frac{\Delta l}{0.5 \cdot (v_i \,+\, v_f)}\,. \tag{1}$$

Here Δl is the EGS4 particle transportation step, and v_i, v_f are particle velocities at the beginning and at the end of the step, respectively.

2.2 Tracking inside Accelerator Vacuum

If photons during their propagation inside the accelerator vacuum simply move along straight lines, the dynamics of charged particles in the regions with nonzero electromagnetic field is more complicated and is governed by relativistic equations of motion. In general, both, fields and particle trajectories, can be found only following some numerical procedures, and in this subsection we shall briefly describe the numerical methods currently used in our calculations.

2.2.1 Equations of Motion and their Numerical Integration

For generating the dynamic of a particle of charge e and rest mass m_0 in a combined external electrical and magnetic field we use the relativistic equations of motion written in the SI unit system

$$\frac{d\vec{r}}{dt} \;=\; \frac{1}{m_0\gamma}\,\vec{p}, \qquad \frac{d\vec{p}}{dt} \;=\; e\vec{E} \;+\; \frac{e}{m_0\gamma}\,\vec{p}\times\vec{B}\,. \tag{2}$$

Here the vectors $\vec{r} = (x,\, y,\, z)$ and $\vec{p} = (p_x,\, p_y,\, p_z)$ are position and kinetic momentum variables, $\vec{E}$ is electric field strength, $\vec{B}$ is magnetic flux density, and t is the time. The Lorentz factor γ in the variables used is given by the expression

$$\gamma \;=\; \sqrt{1 \;+\; \frac{|\,\vec{p}\,|^2}{m_0^2\,c^2}} \tag{3}$$

where c is the speed of light in vacuum.

The main difficulty in the numerical integration of the equations (2) is to approximate the particle motion in the high-gradient time-varying cavity field for many rf-periods. This problem should be treated as a stiff problem, and the general recommendation in that case is to use implicit numerical methods, because explicit algorithms will have severe stability limits on the step size. But for the particle motion in a cavity where the evaluation of fields is rather expansive (see detailed description below), it is better to use another standard practice and compare the numerical work not by the number of steps but by the number of field evaluations. From this point of view the computational cost per step of an implicit method is definitely higher than that of an explicit method because it involves the solution of

some system of, generally speaking, non-linear algebraic equations. Taking additionally into account that implicit methods can not well be combined with adaptive algorithms, and that in embedded explicit methods the number of field evaluations can be essentially reduced by using variable step sizes (small step sizes when the solution changes rapidly and large step sizes when the solution is only slowly varying), we have chosen and implemented an explicit fifth order embedded (error estimator of order four) Runge-Kutta method of Dormand and Prince with an automatic choice of the stepsize following the recommendations in [24], [25]. The continuous forth order output of this integrator greatly helps for the precise determination of the particle impact coordinates.

Note that it is now well known that numerical methods such as the ordinary Runge-Kutta methods are not ideal for integrating equations of motion of charged particles, because the system (2) is not generic in the set of all dynamical systems, it is divergence-free and hence preserves the phase space volume during propagation along particles trajectories. Numerical approximation may introduce unphysical dissipative perturbations into the original problem and it should result in a completely different long-term behaviour. Unfortunately, except for some special cases, general mechanical integrators[1] cannot be explicit (see, for example [26], [27]) with all already discussed above consequences of it. So, having implemented in our computer code a nonmechanical integrator, we share the wide-spreaded viewpoint that the main interest of mechanical integration is in long-time integrations; for short-time integration it plays no role and a good method is one with small local errors.

In the near future we plan to supplement our code with some mechanical integrator (to study, for example, dynamic of captured particles or design beam failure), and currently we never follow particles on distances larger than a few FODO cells, and use, in average, 40-50 numerical integration steps per rf-period.

[1]Numerical integration schemes for differential equations which preserve some qualitative properties of original system (symplecticity, first integral, phase space volume, and so forth) [27]. The corresponding area of numerical analysis is now called geometric integration.

2.2.2 Calculation of Fields

Every element in our code must be declared as field equipped or field free element. If the element is declared as field equipped, it must be supplied with a subroutine, which will provide the actual values of the electromagnetic field inside the element at a given space point and time moment.

There are mainly two types of fields in which we are interested for particle dynamic simulations in the TESLA main linac: magnetic fields of focusing quadrupoles and accelerating fields of TESLA cavities. For the calculations presented in this paper we used a simple analytical model for the quadrupole field: a magnetic field, linear with respect to the transverse coordinates and independent of the longitudinal position, which abruptly falls to zero outside of the effective length of the magnet and outside the beam vacuum. For the TESLA cavity, where no analytical solution for the field is available, we have to relay on some numerical method for the field calculation. Currently, we take the cavity field imported from the 2D FEM code of J.Sekutowicz [37]. This code approximates the cavity domain with the help of an irregular triangular mesh which is constructed from two types of triangles: straight triangles and triangles with one curvilinear side. Such accurate description of the inner shape of the cavity gives us hope that we will have correct electromagnetic fields near the cavity walls, which is important for our simulations. A part of the mesh used for the actual field calculation and how it fits into our material model of the TESLA cavity, can be seen in figure 1.

An additional reason to use the output of Sekutowicz's code for the electron trajectory computation was that a specially written program for reading data files, for finding mesh triangles in which a given point is located, and for producing resulting field values was available [18]. Unfortunately, numerical experiments have shown that this program was too slow to be used in our code. So it was practically completely rewritten with greatly increased performance speed.

2.3 Some General Code Design Questions

In this subsection we will mark briefly some additional code possibilities which were not discussed in the above description.

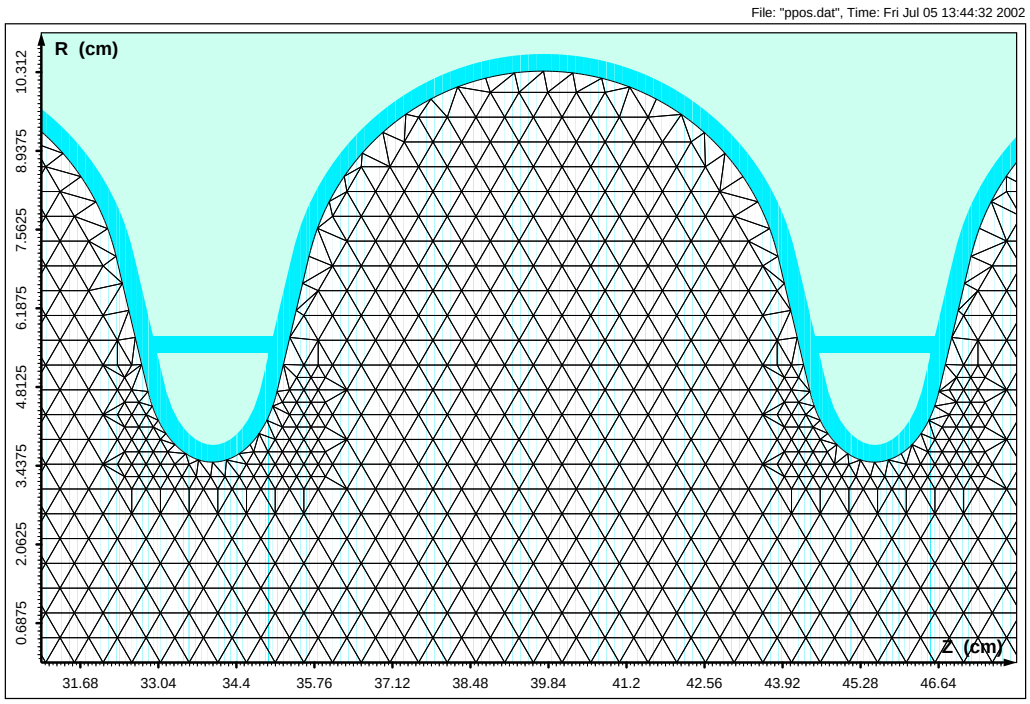

Figure 1: A mesh used for the electromagnetic field calculation of a 1.3 GHz TESLA accelerator cavity.

2.3.1 Generation of Primary Events

Formally, the input particles are supplied by a special subroutine named InpNextP, which, actually, has to be written by the user reflecting his specific needs. Also it is possible to read particles from a file, or use one from the already implemented particle generators, which will be discussed below in this paper.

2.3.2 Particle Generation Number

As an additional particle coordinate we have introduced the particle generation number, which is a positive integer and serves to show how many impacts of the inner vacuum surface of the accelerator happened in the particle history traced backwards up to input particle.

Particles of first generation will be called primary particles. All other particles will be called shower secondaries.

2.3.3 Particle Weight and Particle Splitting

For each input particle we assign some weight $W > 0$, which then can be used and modified during simulations. For example, to increase the statistical robustness, a particle, when it impacts accelerator material, can be splitted into N identical particles each with weight W / N. The splitting number N can be chosen to be a function of the particle generation number.

2.3.4 Primary Impact Energy and Deposited Energy

When a first generation particle impacts the inner vacuum surface of an element, its energy (kinetic energy for electrons) is added to the counter of the primary impact energy of the element. Besides that, independently from the particle generation number, the actual energy deposited in every element material is recorded.

2.3.5 Output and Graphical Output

After every program execution a run summary is produced. It contains information about the number of input particles; initial energy and energy gain from electrical fields; deposited into accelerator materials and primary

impact energies; and many other run statistics, including an energy balance check.

Particles, which reached marked places in the accelerator (for example, its exit or entrance) can be saved in user specified files, if necessary. Then these files can be used as input for the next run, or can be analyzed with the help of a specially written program, which is also able to produce directly different postscript plots of particle distributions (as examples, see figures 9, 10, 11, 12 and 13 produced by this program).

Besides that the encoded geometry can be plotted, showing materials and, if necessary, the mesh used for field calculations; it is a valuable tool for checking complex geometries before execution. Particle trajectories, EGS4 interaction points, and EGS4 particle discard points also can be shown. One can specify a color legend for representing different materials and chose trajectories plotting of electrons, positrons and photons with different colors (as examples, see figures 1, 8 and 5). So most of the pictures in this paper were produced by the graphical possibilities of our code.

3 TESLA Main Linac Model

The TESLA main linac model created for simulations can be divided into two relatively independent parts, electromagnetic field models and material geometry. Field models were already discussed in the previous section, and in this section we will describe the material model used in our calculations. First we will introduce basic elements, after that we will construct standard linac cryomodules from these elements, and then we will form the material models of FODO cells and of the whole TESLA main linac.

3.1 Basic Elements

We assume that adequate estimates of the development of electromagnetic cascade showers in the TESLA main linac can be obtained from a simplified axisymmetrical approximation of its material geometry. This assumption does not change the material geometry too much and is very helpful. Firstly, it simplifies significantly the internal program logic and thus increases the speed of numerical computations and reduces the number of possible implementation bugs. Secondly, this allows the simulations inside a chain of cavities to be started in a single (longitudinally axis-centered) plane, where

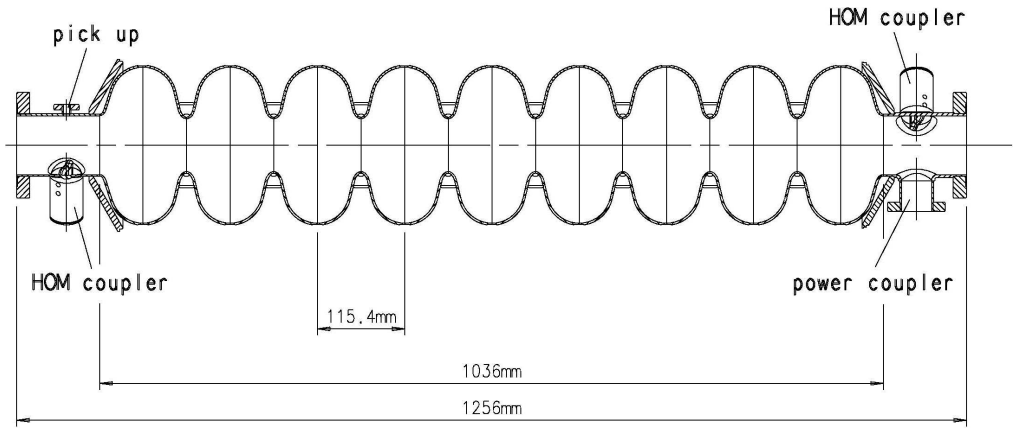

Figure 2: Side view of the 9-cell TESLA cavity with the main power coupler and two higher-order mode couplers [1].

the resulting particle distribution at the cavity chain exit will be rotated about the linac axis for further tracking, which reduces the initial number of particles required for a statistically robust study. Approximations which we made creating axisymmetrical material models of the TESLA main linac elements can be seen by comparing drawings taken from the TESLA Technical Design Report (TDR) [1] and pictures produced by the graphical output of our program.

3.1.1 Cavity

The TESLA cavity is a 9-cell standing wave structure of about $1\,m$ length whose fundamental TM mode has a frequency of $1.3\,GHz$. The cavity is made from solid niobium and is bath-cooled by superfluid helium at a temperature of $2\ K$. Its side view taken from the TDR can be seen in figure 2. Note, that the entrance and the exit cavity half-cells have shapes which are slightly different from each other and from the shapes of all remaining half-cells, which are identical.

In our material model the RF power coupler and the two high order mode (HOM) couplers at the end sections of the cavity are not considered, and are replaced by the beam pipe of an inner radius of $3.9\,cm$ made from niobium. The whole material model of the TESLA cavity in our program consist of a niobium cavity encapsulated in titanium vessel filled with liquid helium, two

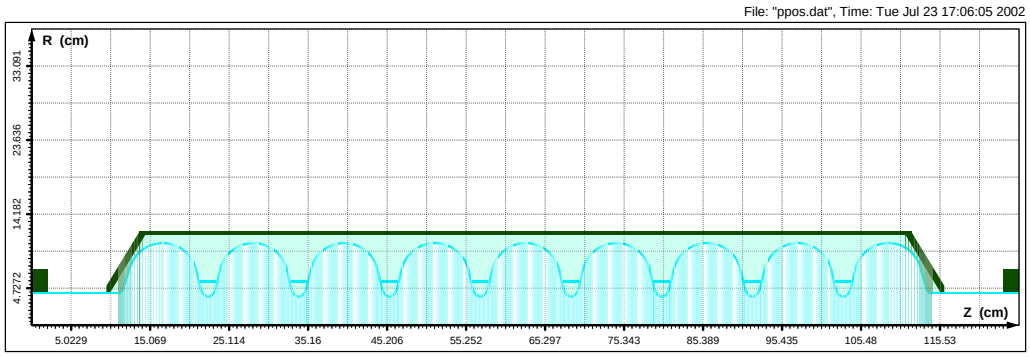

Figure 3: The material model of the TESLA cavity with end sections and flanges.

niobium end sections at both sides, and two stainless steel flanges at both end sections (see figure 3).

3.1.2 Quadrupole Package

To simplify the material geometry of the designed TESLA quadrupole package (figure 4) we have not taken into account the correction coils for vertical and horizontal beam deflection, and changed the quadrupole coils to be a solid copper cylinder. The resulting model can be seen in figure 5.

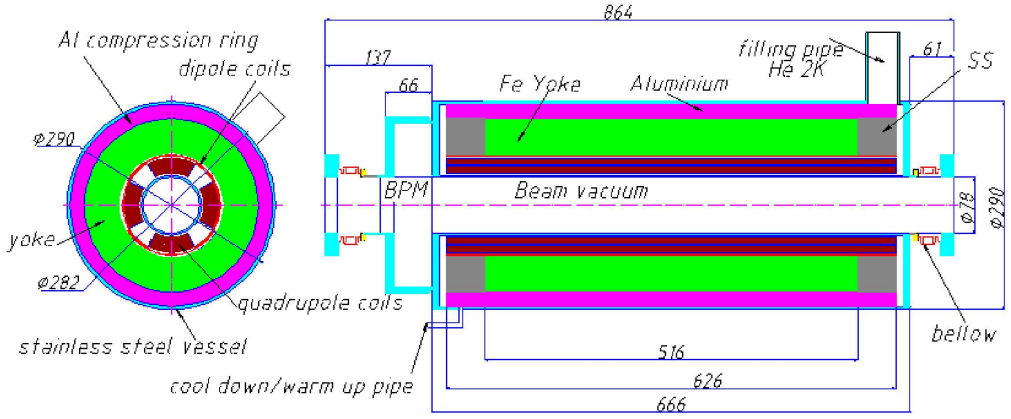

Figure 4: The cross-section and longitudinal cut of the superconducting quadrupole package for the TESLA linac [1].

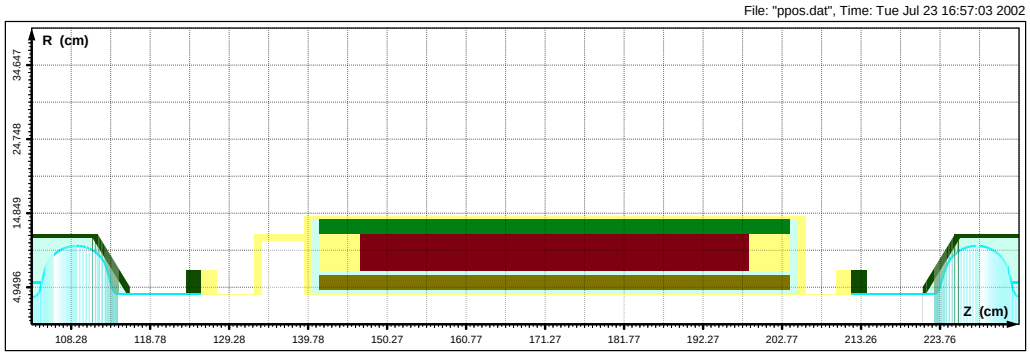

Figure 5: The material model of the quadrupole package. The end section and one cell of the neighbouring cavities are also shown.

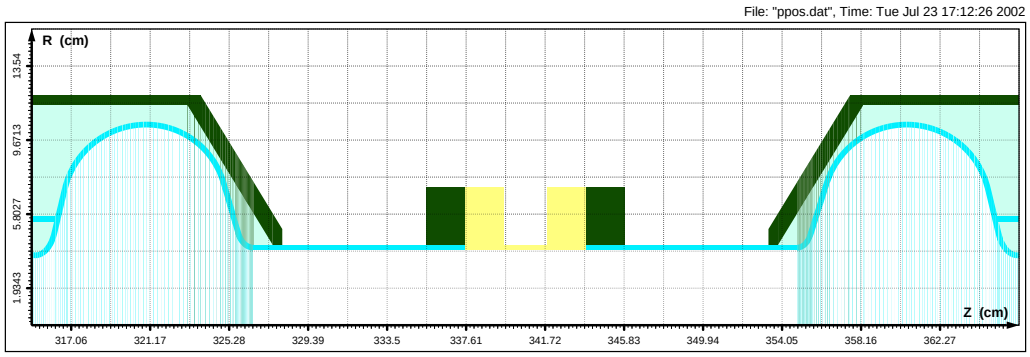

Figure 6: The material model of the inter-cavity section.

3.1.3 Inter-Cavity Bellows and Cryomodules Interconnection

Within the cryomodule the cavity end sections are joined by flanged bellows, which in our model are replaced by a stainless steel beam pipe with flanges.

The interconnection between cryomodules consists of a $38\,cm$ long section and incorporates a higher order mode absorber, a bellow, and a vacuum pumping port which are not considered in the current material model: the interconnection section is modeled as the beam pipe with flanges at both sides.

Figure 6 shows the material model of the bellow with flanges, the cryomodules interconnection section has the same view, only the length of the pipe between the flanges is longer.

3.2 Standard Linac Modules and TESLA Lattice

Having introduced four basic elements, we can now construct the simplified material model of the TESLA main linac. It will include all media between the inner vacuum surface and the outer surface of the helium vessel for the cavities and quadrupoles, inter-cavity bellows, and cryomodules interconnection sections. All other equipment placed in the cryomodules will not be taken into consideration.

3.2.1 Accelerator Modules (Cryomodules)

In accordance to the TDR [1], we have constructed two types of standard accelerator modules (cryomodules) from the basic elements, CMOD1 and CMOD2. The cryomodule CMOD1 is constructed from 12 cavities, 11 inter-cavity bellows, and one interconnection section at the end of the module (for the interconnection between modules). The cryomodule CMOD2 is a module with an additional quadrupole package, which is located at the centre of the module.

3.2.2 FODO Cells and TESLA Lattice

The beam is focused in the TESLA main linac by means of a FODO lattice: FODO1 cells, which are used for beam focusing in the energy range from 5 to $125\,GeV$, and FODO2 cells for a beam energy range from 125 to $250\,GeV$.

The FODO1 cell is constructed from four accelerator modules, two of which have an additional quadrupole package

$$\text{FODO1} = (\text{CMOD2, CMOD1, CMOD2, CMOD1}).$$

The FODO2 cell is constructed from 6 standard modules, two of which have an additional quadrupole package

$$\text{FODO2} = (\text{CMOD2, CMOD1, CMOD1, CMOD2, CMOD1, CMOD1}).$$

Note, that the constructed model corresponds to the baseline design of the TESLA main linac, which uses the existing 9-cell TESLA Test Facility (TTF) cavities (each cavity is equipped with its individual power coupler) but with reduced length of the interconnection section. The superstructures proposed for the main linac are not considered in this paper. As concerning the focusing properties, the first 40 FODO cells in the linac have a phase advance of 45° per cell, and all remaining FODO's are cells with 60° phase advance[2]. The nominal accelerating gradient was taken as $\simeq 24\,MV/m$, and

[2]In the TESLA design with an integrated X-Ray Laser Laboratory it was proposed to use the first part of the linac (about 40 FODO cells) to accelerate the beam for the X-Ray Facility in an interleaved pulse mode with the collider beam. At low FEL energy operation, a reduction of the phase advance from 60° to 45° per cell for the high-energy beam is necessary to avoid over-focusing of the lower-energy FEL beam. So in this paper we consider the 45°-lattice for the first 40 FODO cells and the 60°-lattice for the last part of the linac (as it will be seen by the high-energy collider beam).

the gradients of the quadrupole magnetic field were calculated for the design injection energy of 5 GeV [1].

4 Modeling Field Emission in an RF Cavity

Field emission of electrons occurs when a sufficiently strong electrical field is applied to a cold metal surface, and is a basic physical effect comparable to thermionic, photoelectric, or secondary emission. Field emission was first observed by R.W. Wood in 1897, and in 1928 R.H. Fowler and L.W. Nordheim provided the first generally accepted quantum mechanical explanation of this effect (see, for example, [28], [2]).

According to the Fowler-Nordheim theory of field emission, the current density j (A/m^2) as a function of the applied accelerating field strength E (V/m) and of the work function of the emitting material ϕ_e (eV) is approximately given by

$$j \;\approx\; A\,E^2\,\exp\left(-\frac{B\,\phi_e^{\frac{3}{2}}}{E}\right)\,, \tag{4}$$

where

$$A \;=\; \frac{e^3}{8\,\pi\,h\,\phi_e\,t^2(y)} \;\approx\; \frac{1.541\cdot 10^{-6}}{\phi_e\,t^2(y)} \tag{5}$$

and

$$B \;=\; \frac{4\,\sqrt{2\,m_0}}{3\,e\,\hbar}\cdot v(y) \;\approx\; 6.831\cdot 10^9\cdot v(y)\,. \tag{6}$$

The exact expressions for the functions $v(y)$ and $t(y)$ can be found, for example, in [29], [30], [31] (references [29] and [30] give also tables of the numerical values of the functions $v(y)$ and $t(y)$ for $y \leq 1$), and the dimensionless parameter y is given by the following formula

$$y \;=\; \sqrt{\frac{e^3 E}{4\,\pi\,\epsilon_0\,\phi_e^2}} \;\approx\; \frac{3.795\cdot 10^{-5}\sqrt{E}}{\phi_e}\,. \tag{7}$$

Note, that although the Fowler-Nordheim equation (4) was obtained for a stationary field, it is accepted that it also delivers reasonable results for RF-fields with frequencies up to several tens of GHz.

Once thought to be explained as a relatively simple quantum mechanical phenomenon, field emission appears to be much more complicated for understanding in practical applications. Measurements have shown, for example, that significant emission can be observed at smaller fields than those predicted by (4) (smaller by factors of the order of 100), and that emission does not take place on the whole surface, but is restricted to small well-localized sites. Different models were considered to explain this and other observed effects (see, for example, [2], [5], [6], [32] [33] and references therein), and one of the most widely accepted is the so-called enhanced field emission model (projection model).

In the enhanced field emission model it was assumed that the increased emission (in comparison to predictions by (4)) must be due to microprotrusions and other defects of the emitter surface, on which the microscopic electric field can be geometrically enhanced by a factor β over the theoretical field calculated for an ideal surface. Thus the enhanced field emission model suggests to use the same Fowler-Nordheim field-current relation, but equipped with two additional parameters, field enhancement factor β and effective emitting area factor S

$$j \;\approx\; S\,A\,\beta^2\,E^2\,\exp\left(-\frac{B\,\phi_e^{\frac{3}{2}}}{\beta\,E}\right)\,. \tag{8}$$

There exist also another point of view on formula (8), where it is suggested to consider β and S as free parameters useful for fitting and then systematizing experimental results without any attempt to connect their appearance with some underlying theoretical model.

4.1 Emission Simulations via Fowler-Nordheim Model

The generation of field-emitted electrons in accordance to the original Fowler-Nordheim model[3] is not a very complicated problem. The distribution of electrons penetrating from a metal into vacuum is known on the metal surface where it can be expressed as function of total and normal to the metal surface particle energies (see for example [35], [36] and [30]). However

[3]Keep in mind, that the original Fowler-Nordheim model for the field emission calculation consists of a semi-infinite slab of a free-electron metal, with work function ϕ_e, and a constant homogeneous electric field applied perpendicular to the planar surface of a metal-vacuum contact.

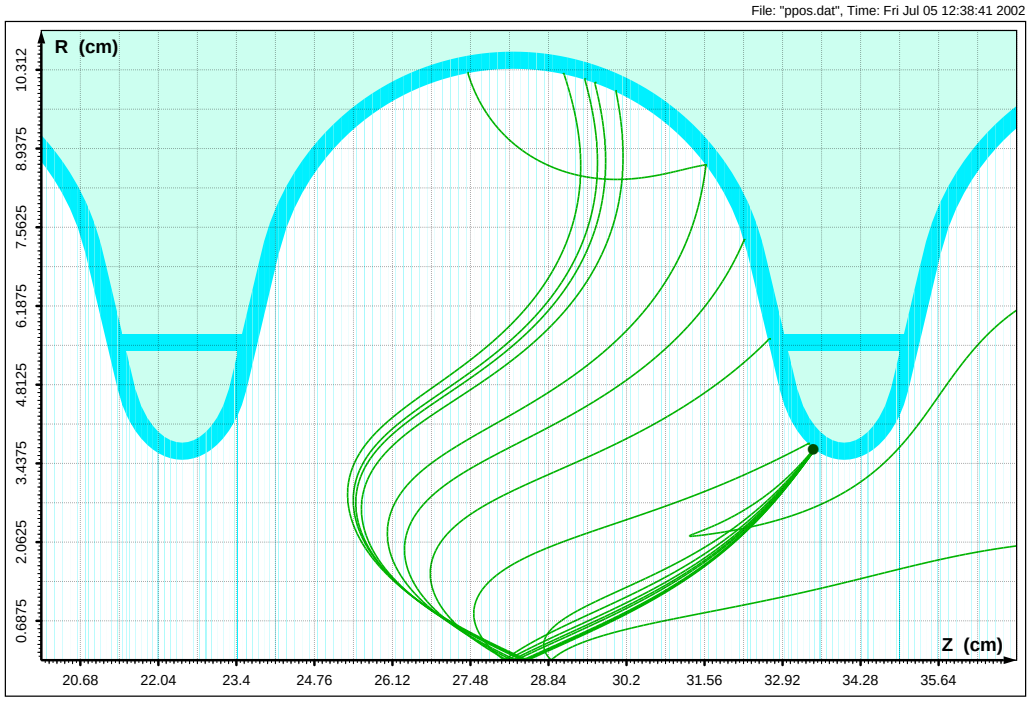

Figure 7: The trajectories of several electrons, emitted with Fermi energy from the same point and in the same time moment, but in different directions. Only the vacuum part of the trajectories is shown. $E_{acc} \simeq 24MV/m$.

tunneling is a quantum mechanical phenomenon and we can not originate classical point-like electrons directly on the plane of metal-vacuum contact, but we can, for example, translate the distribution function into the vacuum on a plane parallel to metal surface[4], where the potential drops down back to the metal level, and generate the electrons here.

Note that the information about the individual energy and direction of emission for each emitted electron is not a point of purely theoretical interest. The effect of a transverse to the surface component of the velocity of the emitted electrons limits, for example, the resolution in field emission microscopy and results in essentially different trajectories for particles moving in a time-varying TESLA cavity field (see figures 7 and 8).

What kind of complications will we meet if instead of the original Fowler-

[4]This can be done because the total energy and parallel to the metal surface momentum are conserved during the tunneling process, and because the considered distribution function does not depend on the position of the emitting point.

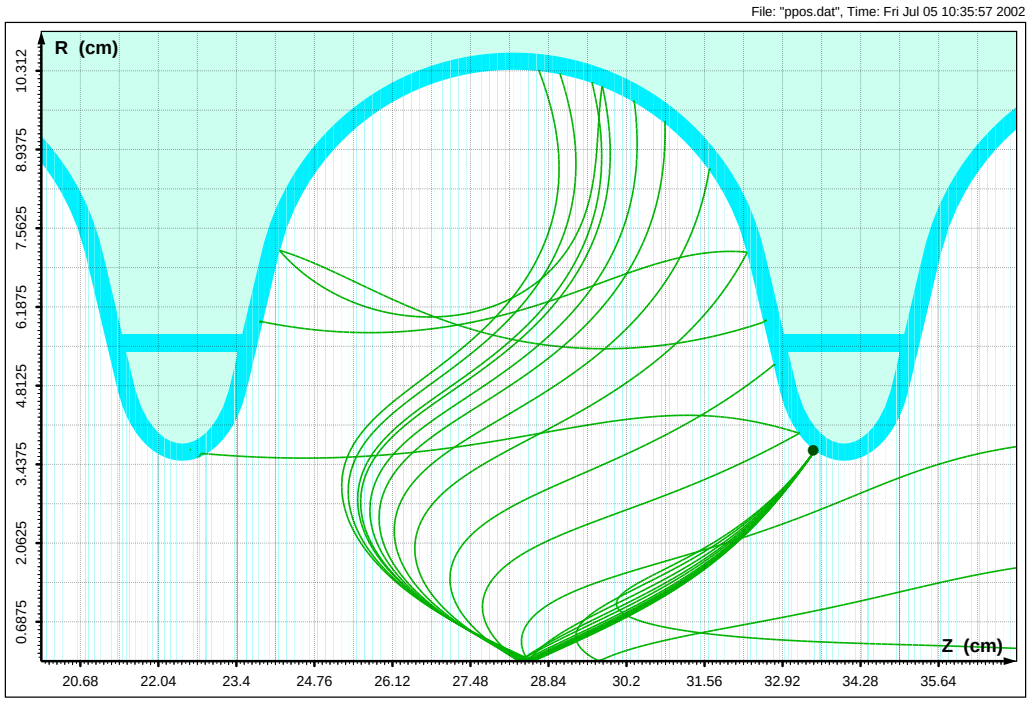

Figure 8: The trajectories of several electrons, emitted with different energies (from Fermi energy down to zero) from the same point in the same direction, and in the same time moment. Only the vacuum part of the trajectories is shown. $E_{acc} \simeq 24MV/m$.

Nordheim model we will try to simulate electron field emission using its enhanced version (8)? Even if we will consistently stay within a pure geometrical point of view, there are no practical reasons to prefer a certain shape of microscopic deformation of the emitting surface and, correspondingly, fix the local geometry and find the local field. So it is probably better to consider both field enhancement factor β and area factor S in (8) as some random quantities whose statistical properties are subject of experimental definition. This approach was already used in [34], where β and S were taken to be independent random variables with distribution functions which do not depend on emitter position and do not evolve in time. Although these assumptions look questionable, having nothing better in mind we will accept them and will start with a description of our procedure of modeling field emission for fixed values of β and S in (8).

- In the considered situation S simply gives a scaling factor, and so, without loss of generality, we will use $S = 1$.

- To be more ensured that we will not miss some rare effect possibly connected with distribution tails, the emitted electrons will be uniformly distributed over the cavity walls and over the half of RF-period in which the electrical field is directed along the inner normal to the cavity surface. At the same time, to satisfy the needed field-current relation, for each emitted particle we will assign a weight proportional to the right hand side in the formula (8).

- The microscopic geometry of the cavity walls and the corresponding local field are unknown, and thus it becomes problematic to use for the simulation the distribution function coming from the original Fowler-Nordheim model. Instead we have used and compared two models of emission direction: emission along inner normal of undeformed cavity walls and model of uniformly distributed emission angles. As concerning the particle starting kinetic energies, they were chosen lying in an interval starting from zero up to some predescribed value, which was varied during numerical experiments[5].

[5]"Typical" emitted electrons have a kinetic energy close to the Fermi energy [35], but because then we trace this electrons in the electromagnetic field calculated for an ideal cavity surface, we, generally speaking, have somehow to simulate the effect of the unknown, locally enhanced field.

- All emitted electrons will be considered as particles of first generation (primary particles). As termination criteria for a single run we will use the requirement to emit some predefined number of particles (10^6 particles for simulations presented in this subsection).

Following the above described procedure we have done a large number of numerical experiments varying β, maximal emission energy and emission direction models, and the main results of our calculations are briefly summarized below. Note, though the presented numbers are related to the cavity accelerating gradient of about $24\,MV/m$, qualitatively we have similar results for other accelerating gradients.

- If the emission conditions (emission direction model, maximal emission energy and EGS4 cutoff energies) are fixed, then the observed relative energies[6] such as deposited in the cavity materials, transmitted transversely[7], released to the cavity exit (entrance) by primary (secondary) particles quickly approach an almost constant values as β increases. These values and energy brought through the cavity exit depend on the emission conditions (for example, changing the emission direction model changes, for $\beta = 100$ and the same emitted current, the exit energy, released through the cavity, by a factor of two.).

- What is more interesting for our purposes, for relatively large β values (larger than $40 - 60$) the particle distributions at the cavity exit (entrance) are practically indistinguishable after appropriate scaling. The dependence on the emission conditions is also very weak (with some additional scaling). Typical particle distributions at the cavity exit can be seen in figures 9, 10, 11, 12, and 13.

- For all relatively large β's in the energy brought to the exit of the emitter-cavity during one RF-period the portion connected to shower secondary particles is about $12 - 18\,\%$, relatively weakly dependent on the chosen EGS4 cutoff energies and particle splitting number. About $65 - 70\,\%$ of this energy are released by particles of the second generation, about $20 - 25\,\%$ by particles of the third generation, about $5 - 7\,\%$

[6] As relative energies we will understand throughout this paper energies measured in the units of the energy brought to the exit of the emitter-cavity during one RF-period.

[7] Energy of particles which have left our cavity material model not through its exit or entrance.

by particles of the fourth generation, and about $2-5\,\%$ by particles of fifth and higher generations.

So accepting the assumptions that the field enhancement factor β and the area factor S can be considered as statistically uncorrelated and typical values of β are of the order of 100, the distribution of particles emitted in accordance with an enhanced Fowler-Nordheim model from a TESLA cavity can be simulated following the above described procedure for a single, relatively large value of β.

4.2 Uniform Emission Model

This paper is not an attempt to give quantities which can be directly compared to experimental data. Our main interest is to see if there are some particles which, being originated near cavity walls, can be captured by the accelerating field or can initiate an amplifying electromagnetic shower. In order to not miss such particles, if they exist, a uniform emission model looks more reliable than the above discussed Fowler-Nordheim type emission model. As it is already almost clear from its name, in this model equally weighted electrons are emitted uniformly over the cavity walls and over the whole RF-period. A detailed view of the resulting particle distribution on the cavity exit (similar to our previous simulations this distribution is again practically independent of the emission conditions) can be seen in figures 14, 15, 16, 17, 18, and 19.

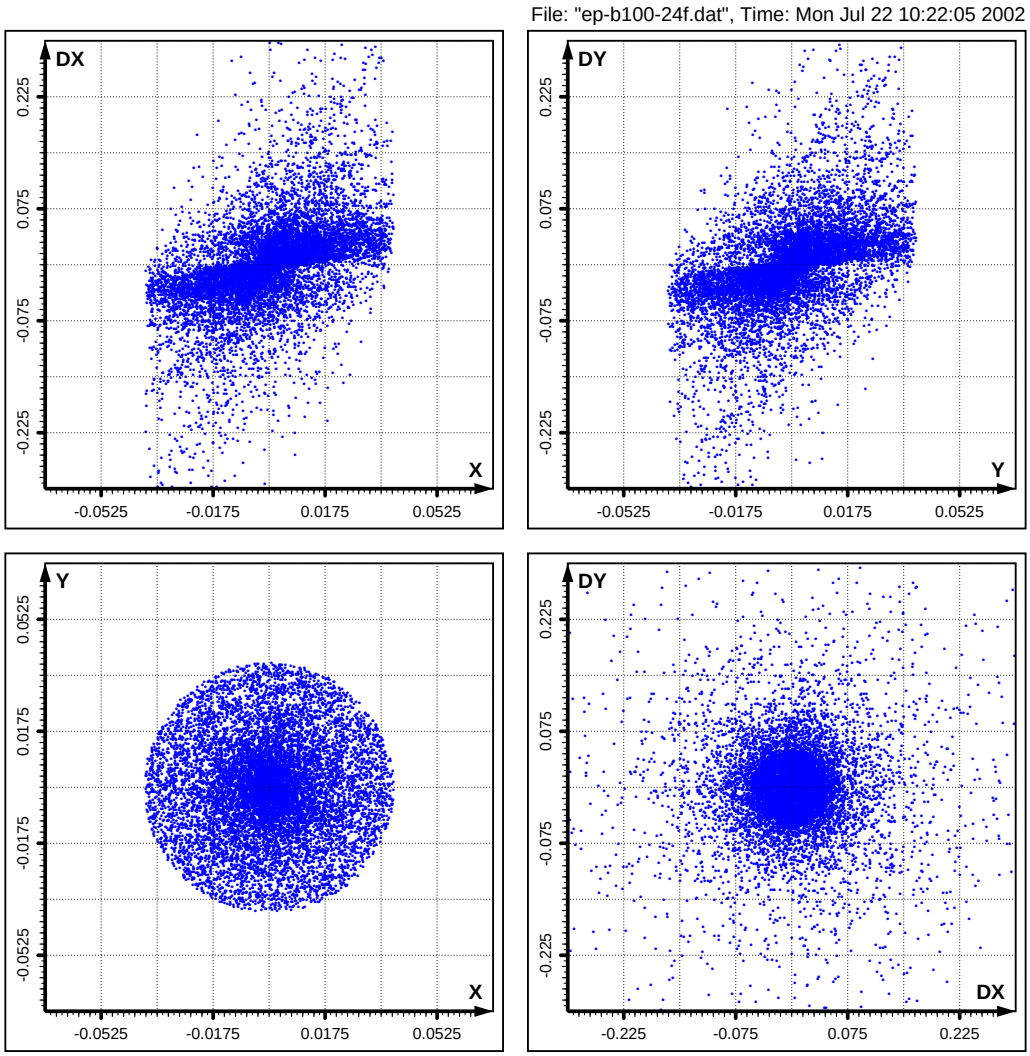

Figure 9: Fowler-Nordheim type emission with $\beta = 100$. Phase space portraits of primary electrons brought to the exit of the emitter-cavity during one RF-period. $E_{acc} \simeq 24\,MV/m$.

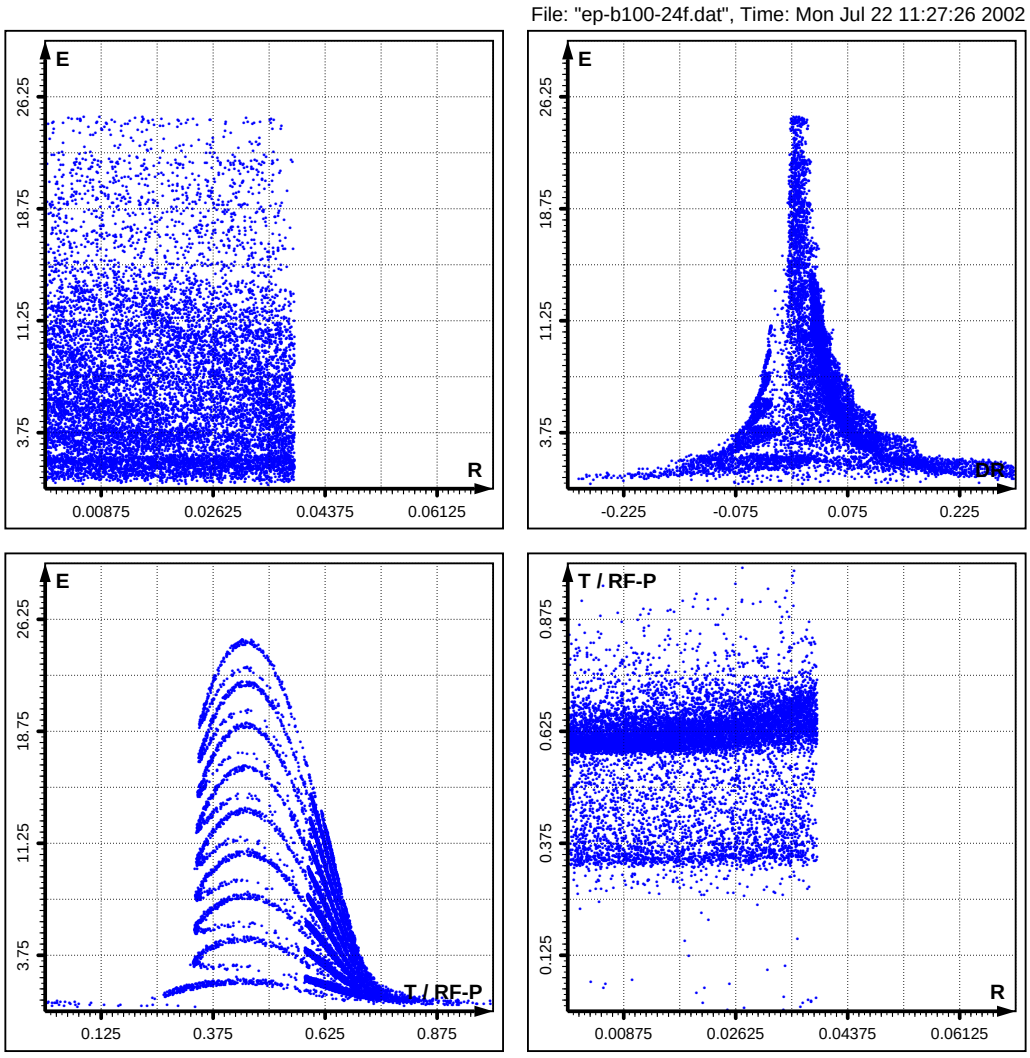

Figure 10: Fowler-Nordheim type emission with $\beta = 100$. Phase space portraits of primary electrons brought to the exit of the emitter-cavity during one RF-period. $E_{acc} \simeq 24\,MV/m$.

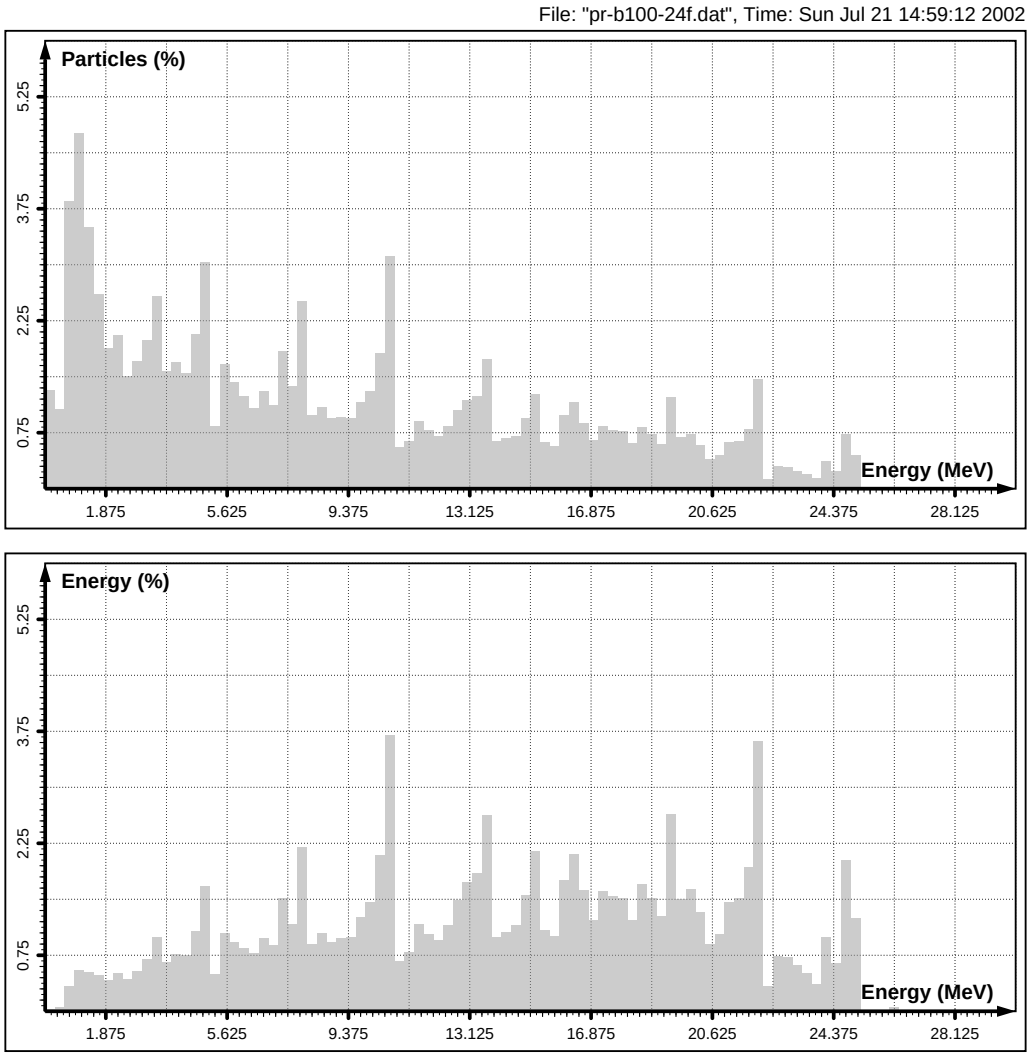

Figure 11: Fowler-Nordheim type emission with $\beta = 100$. Distribution of particles and particle energies on the exit of the emitter-cavity. $E_{acc} \simeq 24\,MV/m$.

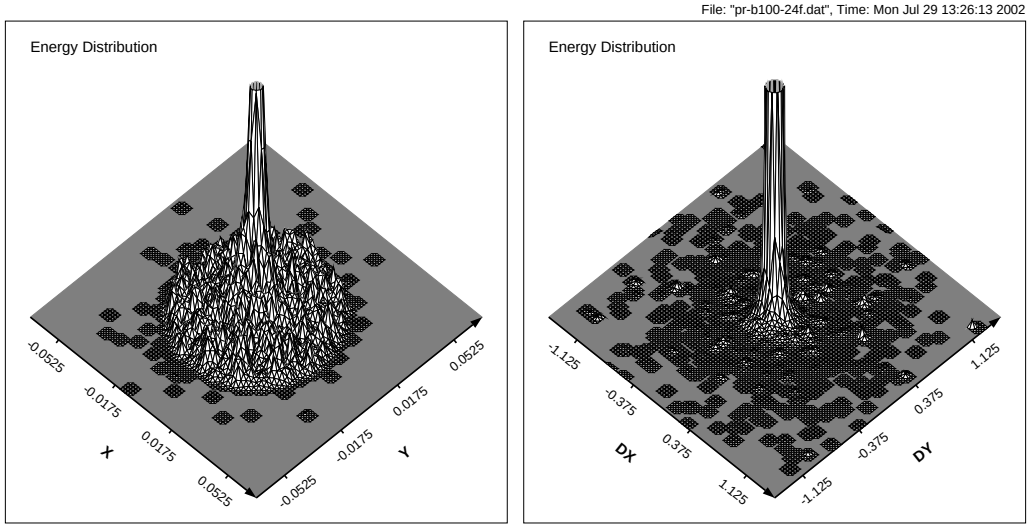

Figure 12: Fowler-Nordheim type emission with $\beta = 100$. Distribution of the energy brought to the exit of the emitter-cavity during one RF-period by primary and shower secondary particles. $E_{acc} \simeq 24\,MV/m$.

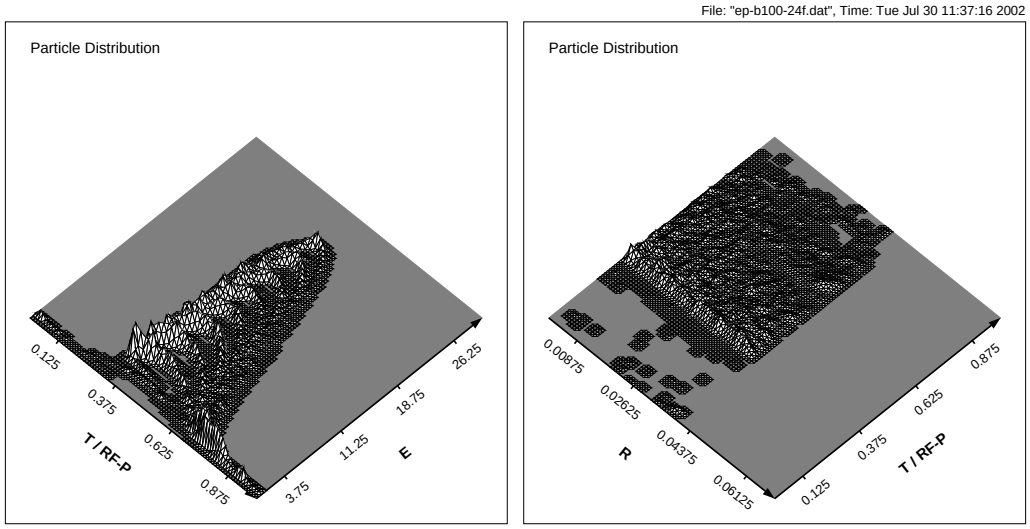

Figure 13: Fowler-Nordheim type emission with $\beta = 100$. Distribution of primary electrons brought to the exit of the emitter-cavity during one RF-period $E_{acc} \simeq 24\,MV/m$.

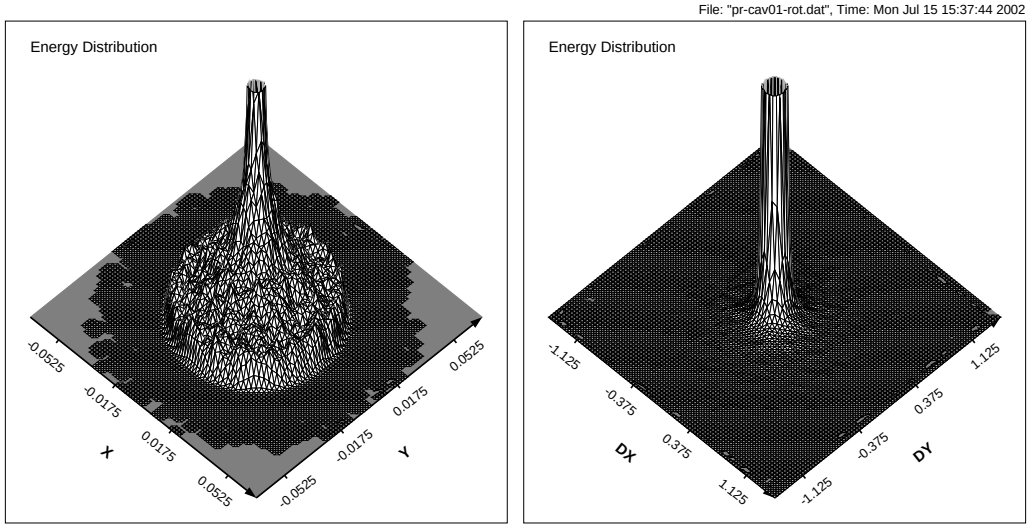

Figure 14: Uniform emission model. Distribution of the energy brought to the exit of the emitter-cavity during one RF-period by primary and shower secondary particles. $E_{acc} \simeq 24\,MV/m$.

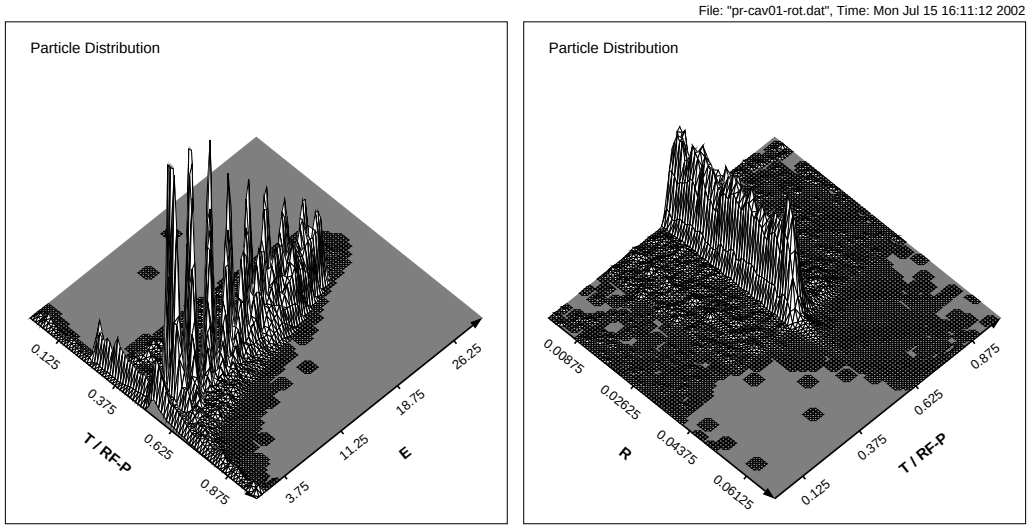

Figure 15: Uniform emission model. Distribution of primary and shower secondary particles brought to the exit of the emitter-cavity during one RF-period. $E_{acc} \simeq 24\,MV/m$.

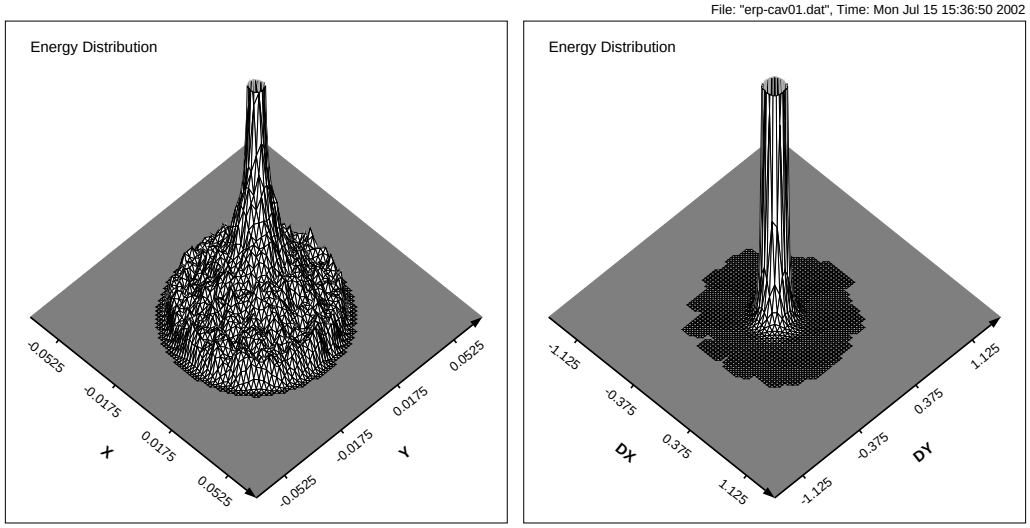

Figure 16: Uniform emission model. Distribution of the energy brought to the exit of the emitter-cavity during one RF-period by primary particles. $E_{acc} \simeq 24\,MV/m$.

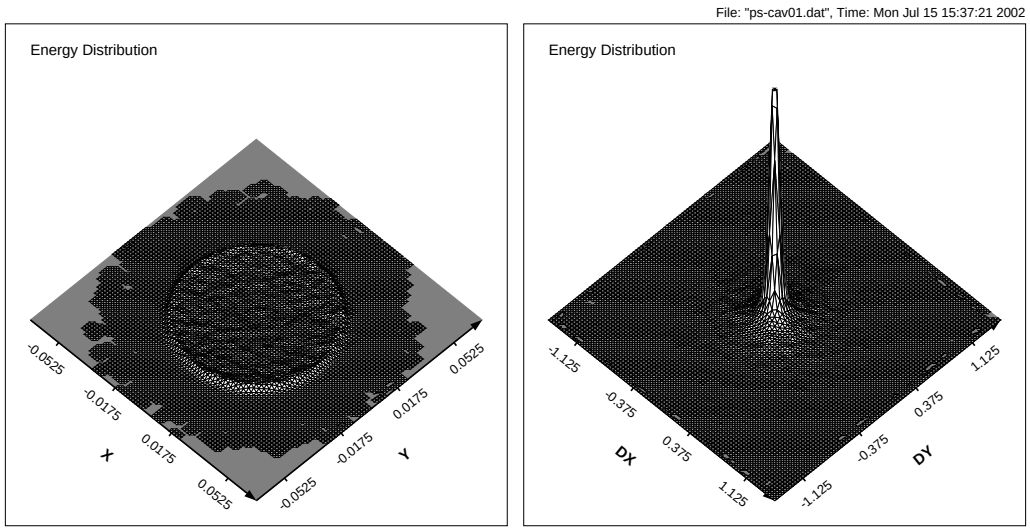

Figure 17: Uniform emission model. Distribution of the energy brought to the exit of the emitter-cavity during one RF-period by shower secondary particles. $E_{acc} \simeq 24\,MV/m$.

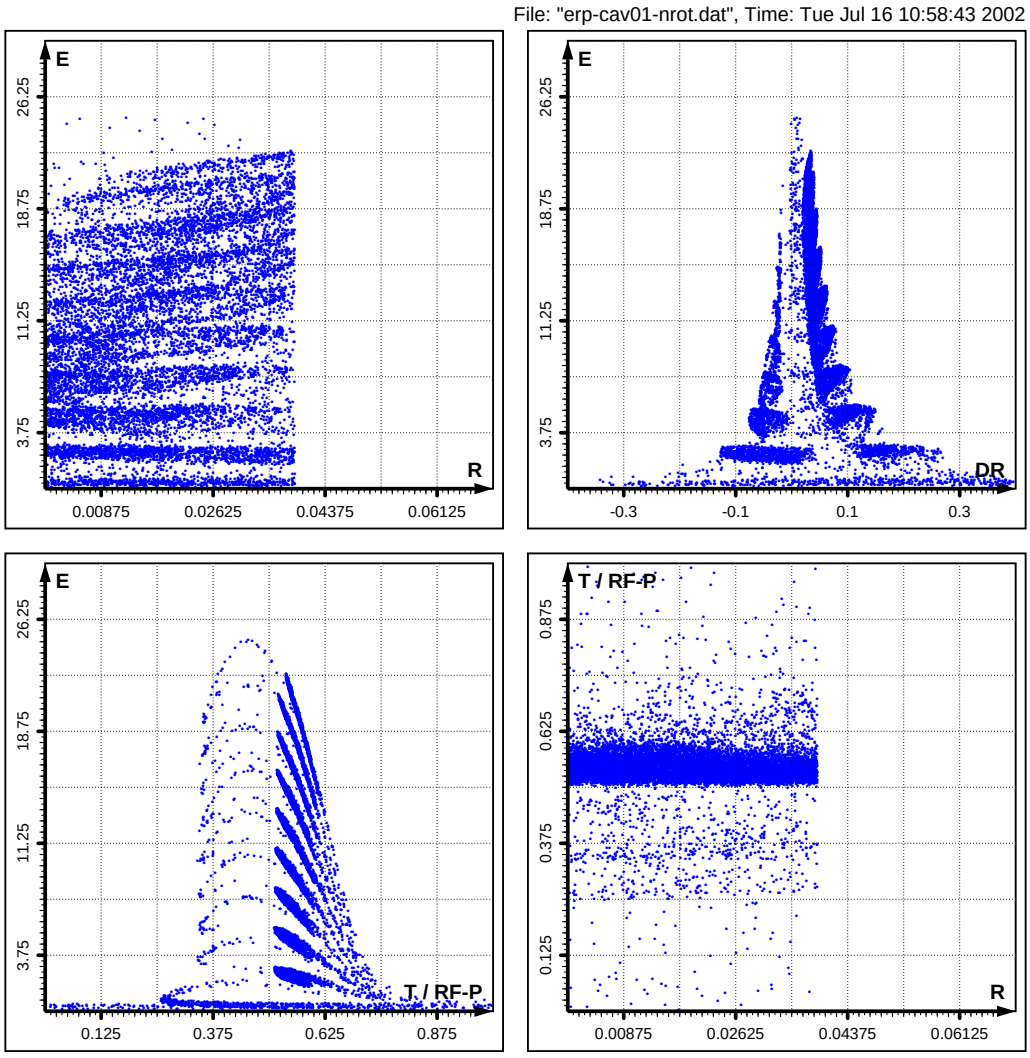

Figure 18: Uniform emission model. Phase space portraits of primary electrons brought to the exit of the emitter-cavity during one RF-period. $E_{acc} \simeq 24\,MV/m$.

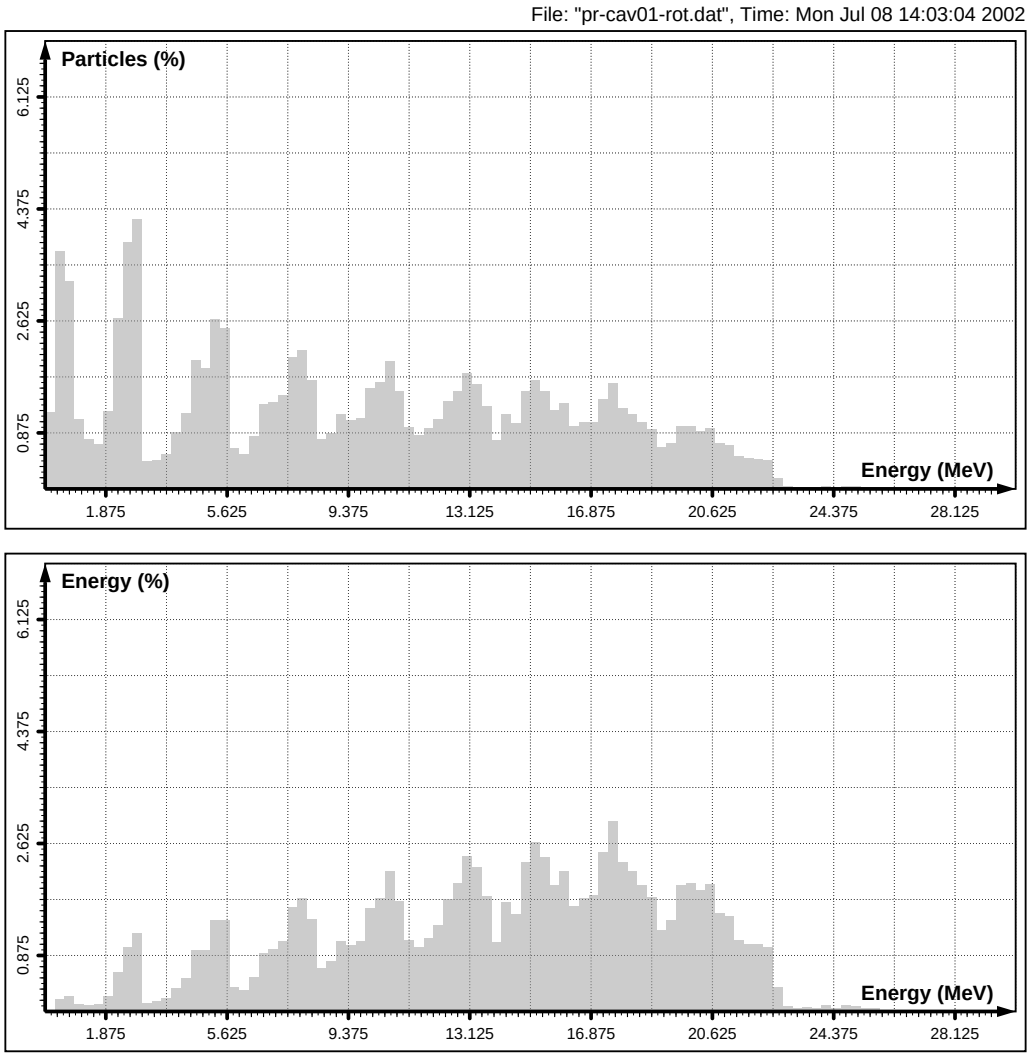

Figure 19: Uniform emission model. Distribution of particles and particle energies on the exit of the emitter-cavity . $E_{acc} \simeq 24\,MV/m$.

5 Simulations of the Behaviour of Field Emitted Electrons and Electromagnetic Shower Development in the TESLA Main Linac

With the help of the developed program we made an extensive numerical study of the behaviour of field-emitted electrons and generated shower secondary particles in the TESLA Main Linac, and our typical calculation procedure can be described as follows.

- We fix some values of the accelerating cavity gradient and the emission model, and then perform an emission simulation until the needed number of particles on both, the cavity exit and the cavity entrance, are collected (usually between 3×10^5 and 10^6 particles).
- We choose a position of the emitter-cavity in the TESLA Main Linac and an injection energy of the high-energy beam, and calculate the quadrupole strengths required to produce the design phase advance of the FODO cells.
- There are two opposite directions in which the emitted particles can be propagated, upstream or downstream along the linac. If we, for example, choose the upstream (downstream) direction, we use for further simulations the particle distribution generated on the exit (entrance) of the emitter-cavity and trace it element by element towards the linac end (start), neglecting on every step particles which were reflected backward with respect to the chosen propagation direction[8].

Note, that all below presented simulation results, especially for the design accelerator parameters, were many times verified by varying such parameters as number of emitted electrons, emission conditions, maximal allowed step of numerical integrator, particle splitting number, and so forth.

[8]In the beginning of our study it was unclear if a possibility exists for something like "cavity to cavity multipactoring due to shower secondaries". After many numerical experiments, we have found that, at least for the design TESLA parameters, it is not the case and we can neglect the effect of backward reflected particles.

5.1 Design Accelerating Gradient and Injection Energy

In our numerical experiments made for the design TESLA parameters ($E_{acc} \simeq 24\,MV/m$ and $E_{inj} = 5\,GeV$) both, primary emitted particles and generated shower secondaries, were deflected transversely and eliminated by quadrupoles, and for each passed cavity the energy deposited in its material model was below the primary impact energy.

As it could be expected from the beginning, particles, which were originated most distant from a quadrupole, had accumulated in average the largest energies before entering the quadrupole and survived the longest distance along the linac. In the first (second) part of the linac we have 24 (36) cavities between neighbouring quadrupoles, and figures 20, 21 and 22 show us, for examples, results of simulations in which for the starting FODO cell the first cavity in the cavity chain is chosen as emitter and the emitted particles are propagated downstream along the linac[9]. In this figures the element number is a relative value, counted from the emitter-cavity, and the filled and empty bars in the upper parts of the plots show the location of horizontally focusing and defocusing quadrupoles, respectively.

To see the process of our simulations in more details, one can look at the following figures, which are related to figure 21: figure 23 shows the relation of the primary impact energy and the actual deposited energy; figures 19, 24, and 25 reproduce the dynamical history of the relative energy distribution; and figures 14, 26, 27, 28, and 29 show the evolution of the energy distribution in the transverse phase space.

Note, that particles which were emitted in accordance to the Fowler-Nordheim type emission model accumulate, in average, the relative energy more intensively, but it does not lead to any serious qualitative differences (see, for example, figures 30 and 31, and compare them with figures 20 and 21, respectively).

In the simulations made for the case when all linac FODO's are cells with 60° phase advance, the particle elimination occurs even a little bit faster due to the stronger focusing.

[9]Particles emitted from the last cavity in the chain and then propagated upstream in the direction of weaker quadrupoles survive, of course, a little bit longer. But the difference is not essential and becomes smaller and smaller when the emitter-cavity is shifted towards the linac end. So all figures presented in this paper will illustrate downstream propagation.

5.2 Effect of Larger Accelerating Gradient

It is interesting to see the threshold in the accelerating gradient after which a multiplication due to shower secondaries becomes a real problem. Because, if this threshold is too close to the design value, we are, probably, not on a safe ground due to the roughness of our simulation model.

The first value of the accelerating gradient where we start to see some qualitative differences[10] is about $100\,MV/m$. Here we have at once two new effects: primary particles emitted in the beginning of the linac seem to be be captured (compare figures 32 and 33), and the actual deposited energy after passing the first quadrupole becomes large than the primary impact energy (figure 34).

An increase of the accelerating gradient to $150\,MV/m$ leads to the situation when shower secondaries start their own life and a multiplication occurs independently of the primary particles, which are either captured and do not impact anymore (figure 35) or are eliminated (figure 36).

Consequences of a further step to the value $200\,MV/m$, which probably do not need any comments, can be seen in figures 37 and 38.

5.3 Effect of Lower Injection Energy

In [38] was pointed, that with lowering the linac injection energy the probability of capturing primary emitted electrons rapidly increases. We have once more confirmed this observation using our new tracking code, and have also looked what happens, if we will simultaneously decrease the injection energy and increase the accelerating gradient (see, as examples, figures 39, 40, and 41).

6 Summary

The main purpose of this study was to answer the question, if a multiplication of parasitic particles due to electromagnetic showers in the accelerator materials can be a problem for the TESLA Main Linac; and the obtained results can be shortly summarized as follows.

[10]Note, that during the scanning of the accelerating gradient we adjust the quadrupole fields appropriately all the time, in order to keep the phase advance of the linac FODO cells unchanged.

- In all our numerical experiments made for the design parameters of the TESLA Main Linac both, primary emitted particles and shower secondaries, were deflected transversely and eliminated by quadrupoles, and for each passed cavity the actual energy deposited in its material model was always below the primary impact energy.

- The design accelerating gradient is well below the threshold after which a multiplication due to shower secondaries becomes a real problem.

- We have once more confirmed the observation of [38], that lowering the injection energy will lead to a capture of primary electrons, emitted in the beginning of the linac, into the acceleration regime.

- The computer code DUST written during this study can be subject of further development to include, for example, secondary electron emission. It also can be used for studying other accelerating structures, and, may be with some minor modifications, for the estimation of the efficiency of collimation systems.

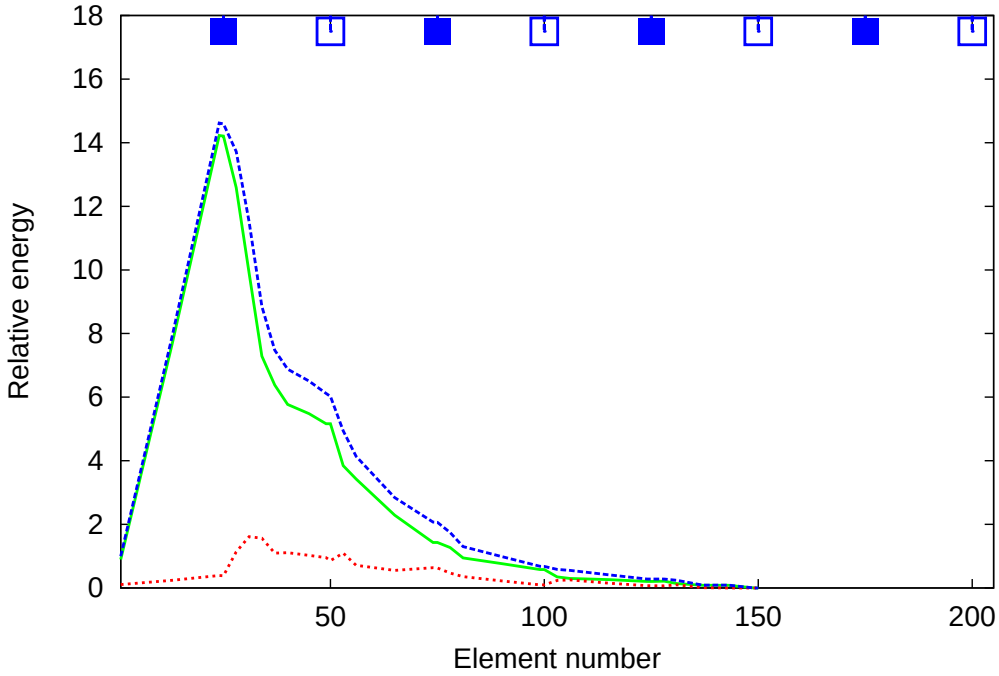

Figure 20: Uniform emission model. Relative energy of primary (solid green), shower secondary (dotted red), and all (dashed blue) particles as a function of the element number. Start in the first FODO cell. $E_{acc} \simeq 24\,MV/m$. $E_{inj} = 5\,GeV$.

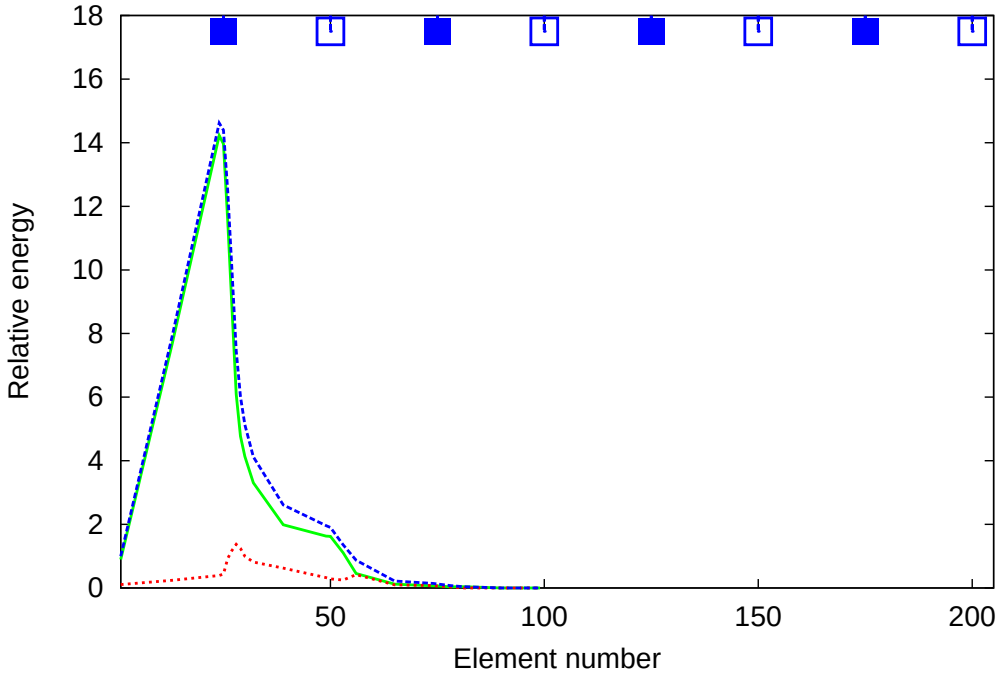

Figure 21: Uniform emission model. Relative energy of primary (solid green), shower secondary (dotted red), and all (dashed blue) particles as a function of the element number. Start in the 9-th FODO cell. $E_{acc} \simeq 24\,MV/m$. $E_{inj} = 5\,GeV$.

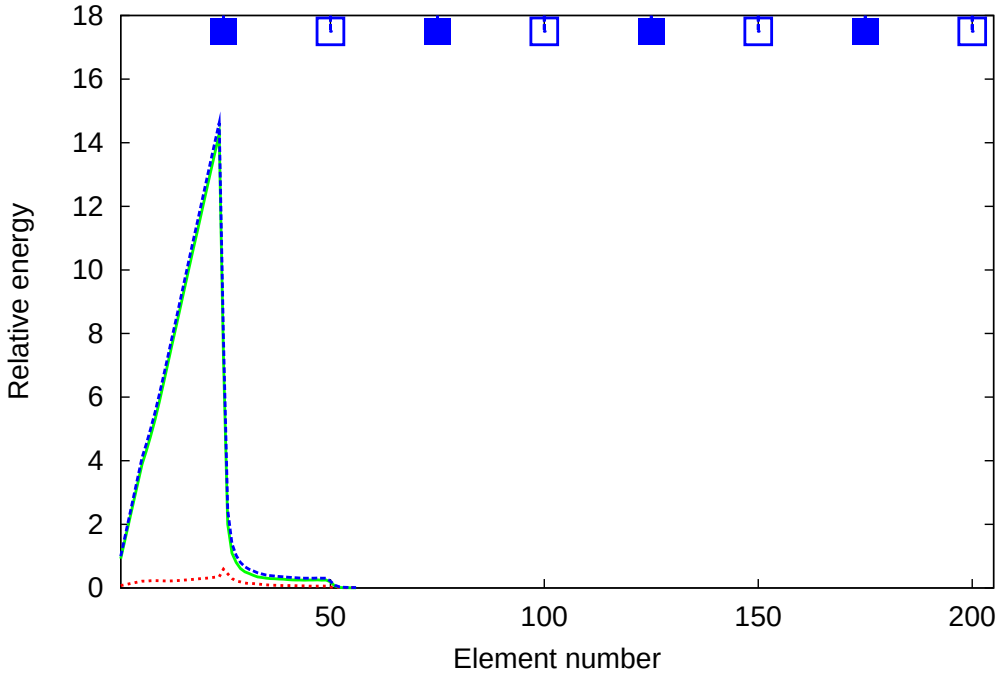

Figure 22: Uniform emission model. Relative energy of primary (solid green), shower secondary (dotted red), and all (dashed blue) particles as a function of the element number. Start in the 95-th FODO cell. $E_{acc} \simeq 24\,MV/m$. $E_{inj} = 5\,GeV$.

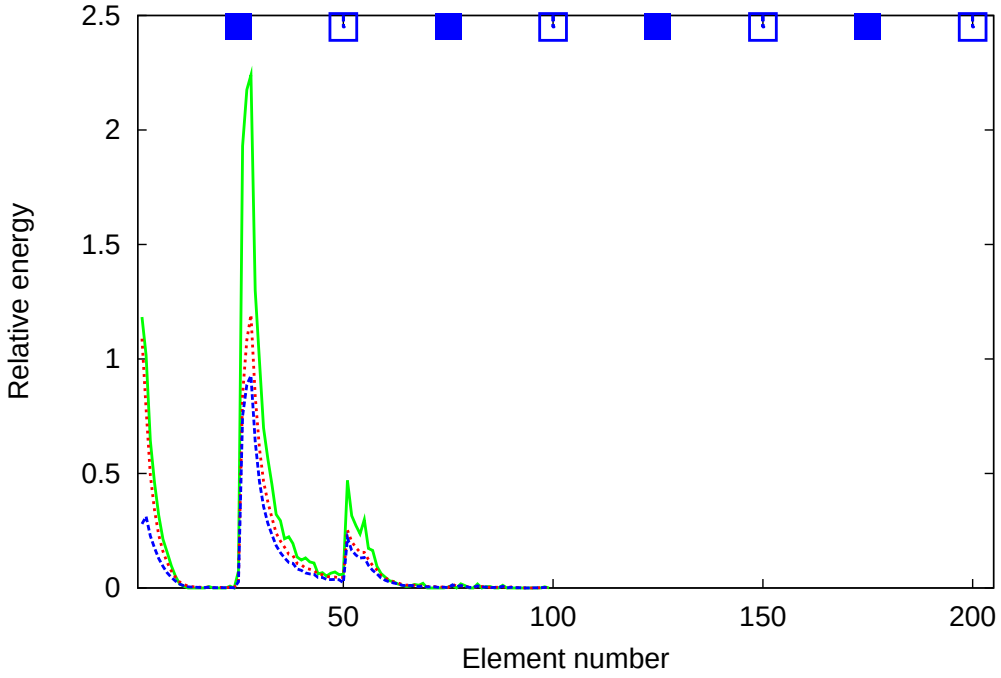

Figure 23: Uniform emission model. Primary impact (solid green), deposited in the element (dotted red), and transmitted transversely (dashed blue) energies as functions of the element number. Start in the 9-th FODO cell. $E_{acc} \simeq 24\,MV/m$. $E_{inj} = 5\,GeV$.

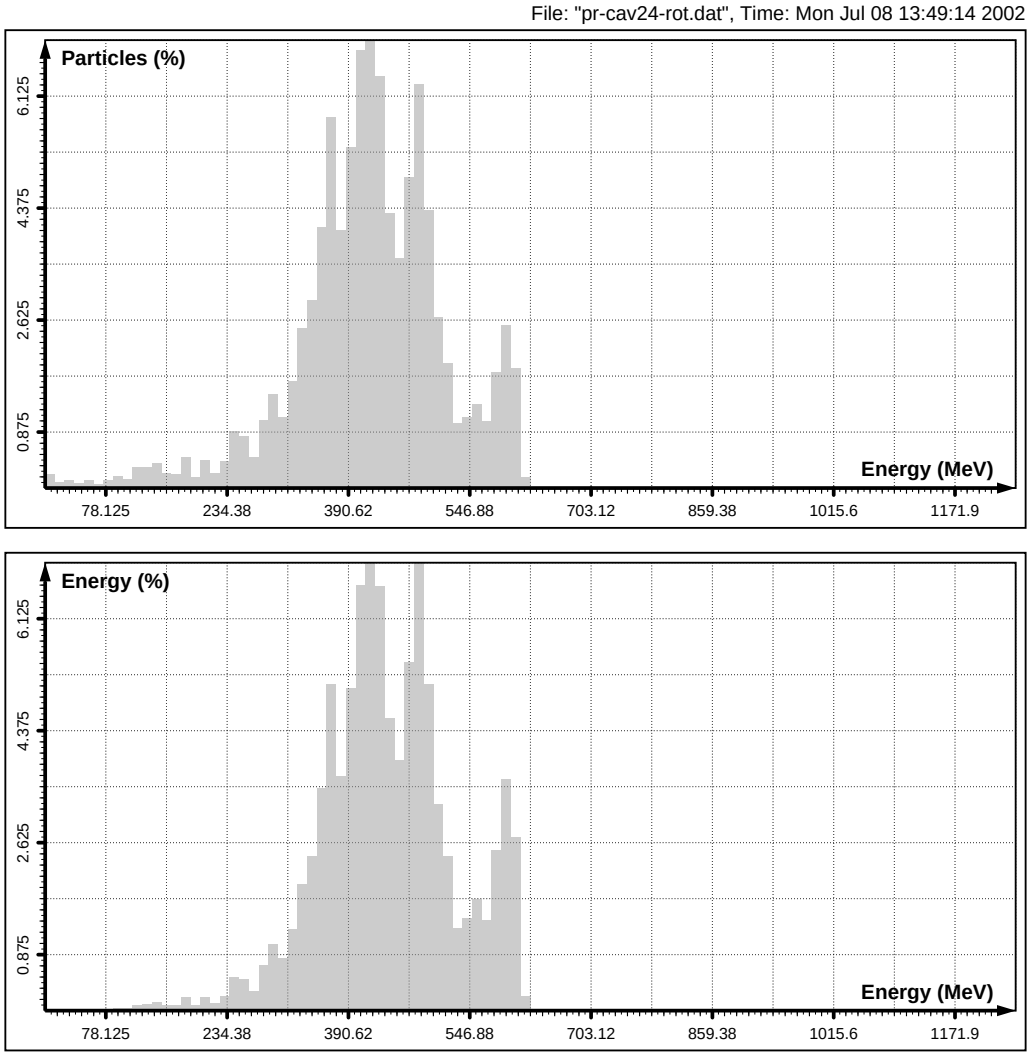

Figure 24: Uniform emission model. Distribution of particles and particle energies at the exit of the first chain of 24 cavities. Start in the 9-th FODO cell. $E_{acc} \simeq 24\,MV/m$. $E_{inj} = 5\,GeV$.

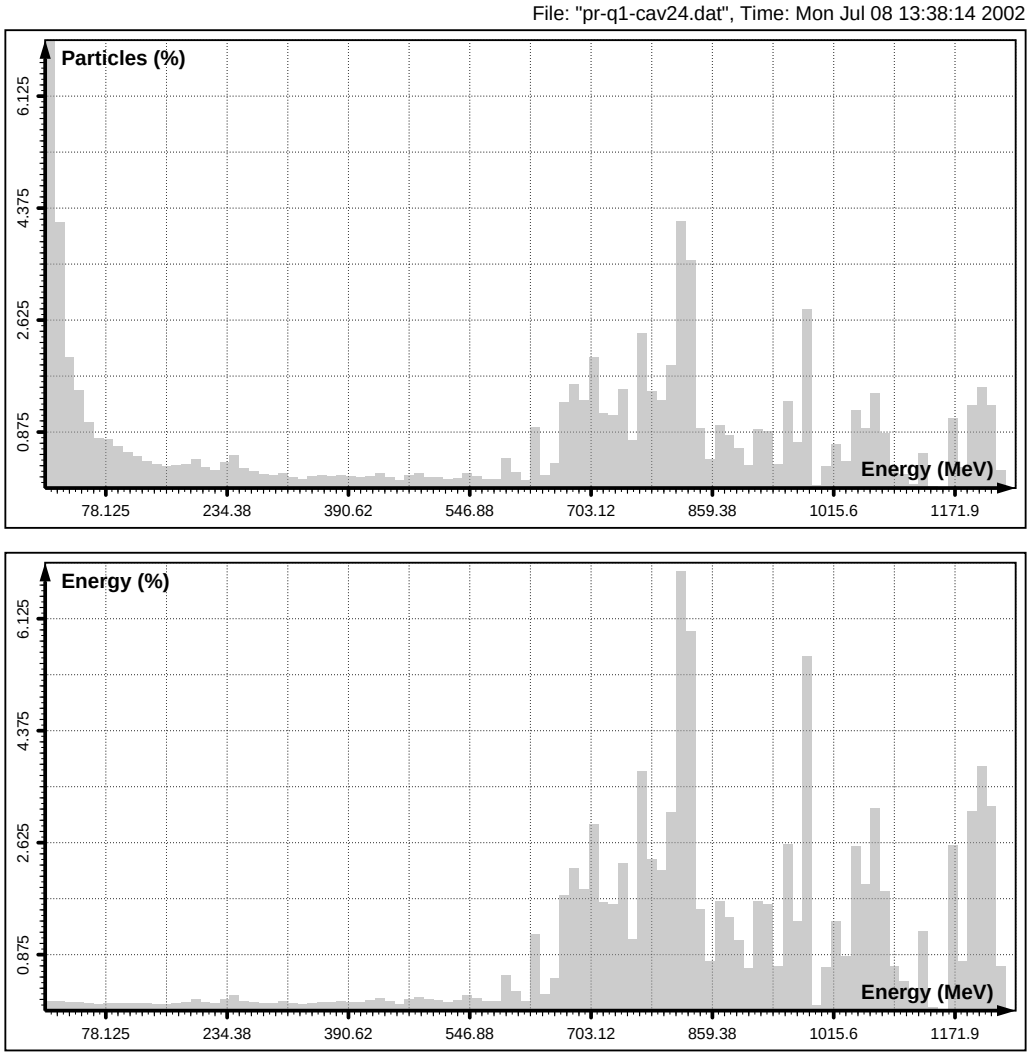

Figure 25: Uniform emission model. Distribution of particles and particle energies at the exit of the second chain of 24 cavities. Start in the 9-th FODO cell. $E_{acc} \simeq 24\,MV/m$. $E_{inj} = 5\,GeV$.

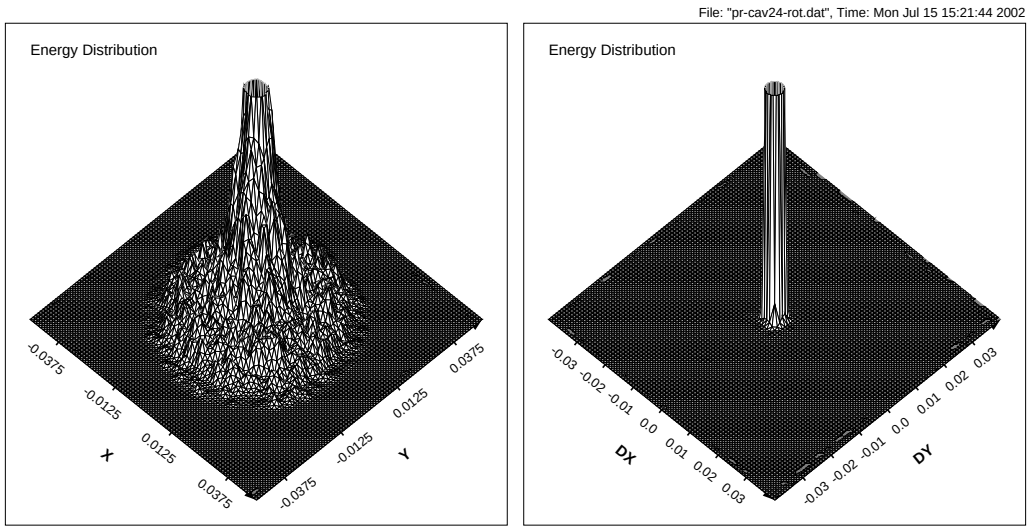

Figure 26: Uniform emission model. Distribution of the energy brought through the exit of the first chain of 24 cavities during one RF-period by primary and shower secondary particles. Start in the 9-th FODO cell. $E_{acc} \simeq 24\,MV/m$. $E_{inj} = 5\,GeV$.

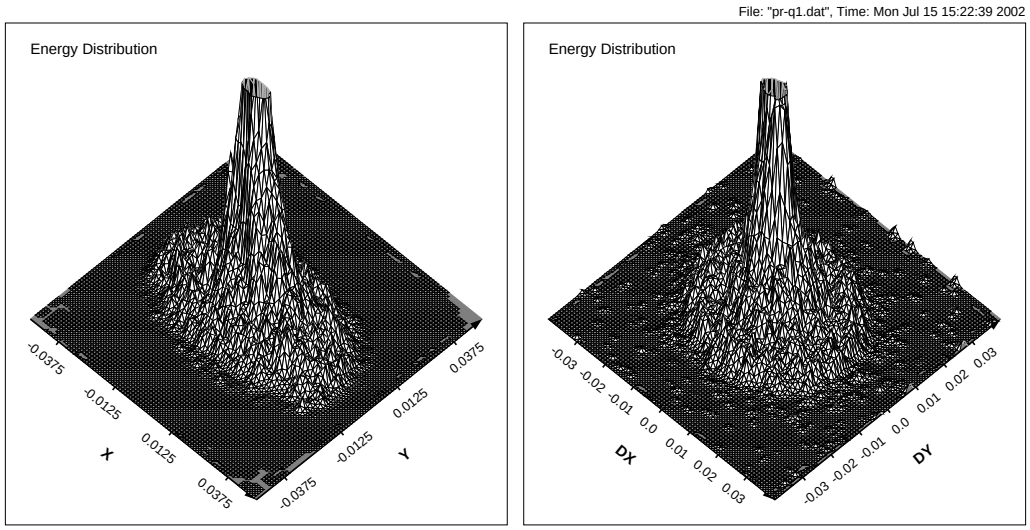

Figure 27: Uniform emission model. Distribution of the energy brought trough the exit of the first quadrupole ($G = 2\,T/m$) during one RF-period by primary and shower secondary particles. Start in the 9-th FODO cell. $E_{acc} \simeq 24\,MV/m$. $E_{inj} = 5\,GeV$.

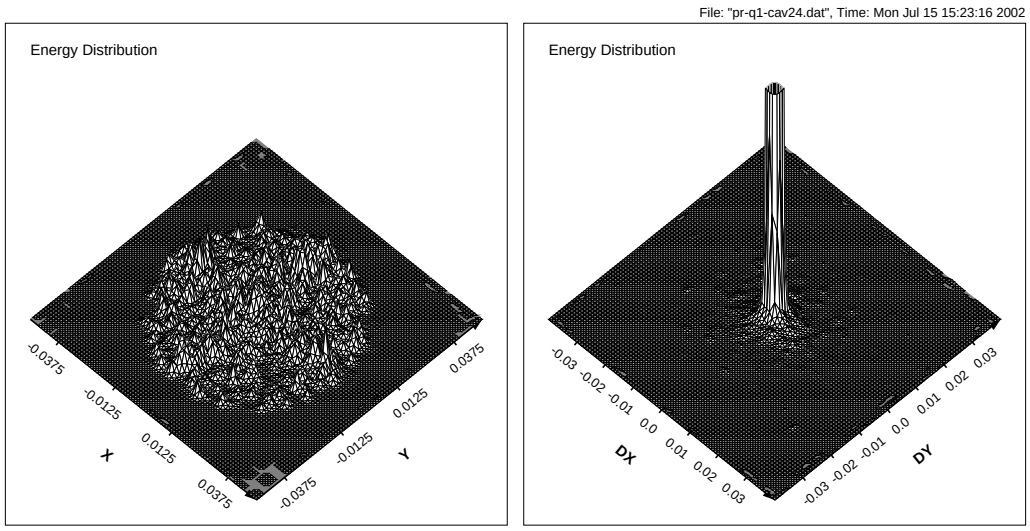

Figure 28: Uniform emission model. Distribution of the energy brought trough the exit of the second chain of 24 cavities during one RF-period by primary and shower secondary particles. Start in the 9-th FODO cell. $E_{acc} \simeq 24\,MV/m$. $E_{inj} = 5\,GeV$.

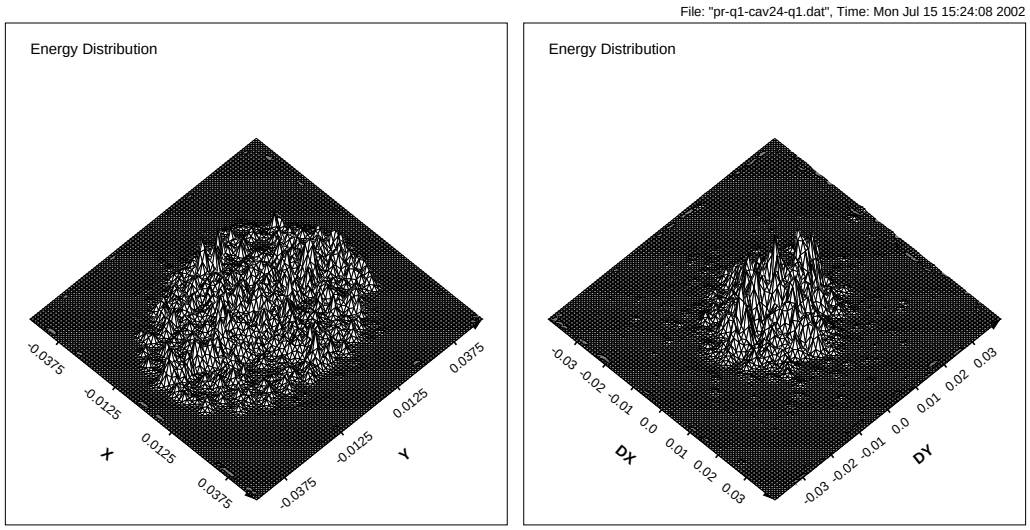

Figure 29: Uniform emission model. Distribution of the energy brought trough the exit of the second quadrupole ($G = -2.1\,T/m$) during one RF-period by primary and shower secondary particles. Start in the 9-th FODO cell. $E_{acc} \simeq 24\,MV/m$. $E_{inj} = 5\,GeV$.

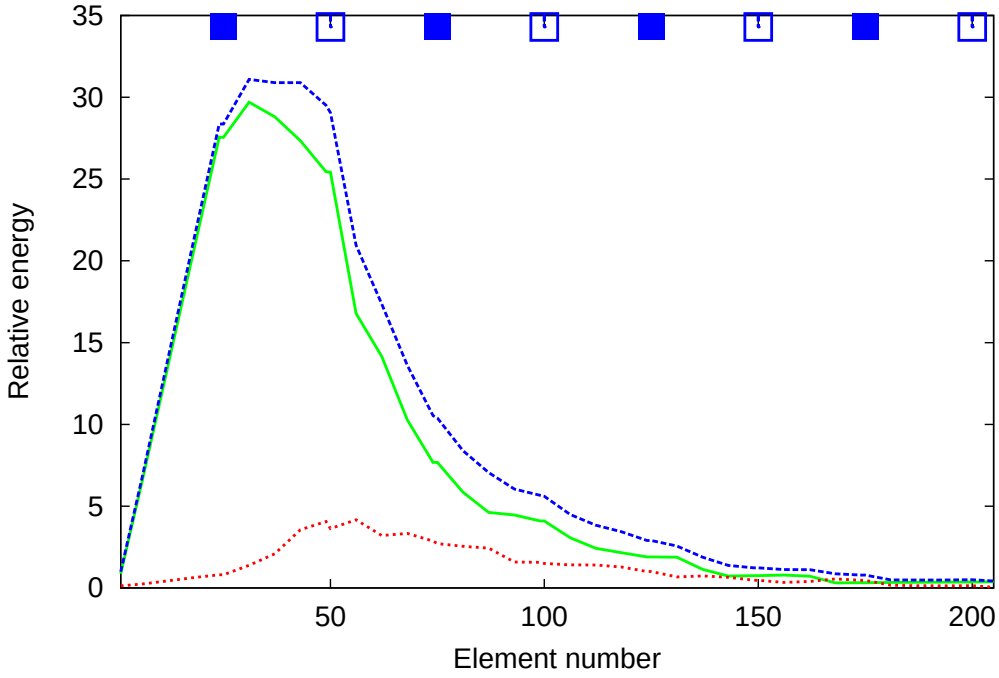

Figure 30: Fowler-Nordheim type emission with $\beta = 150$. Relative energy of primary (solid green), shower secondary (dotted red), and all (dashed blue) particles as a function of the element number. Start in the first FODO cell. $E_{acc} \simeq 24\,MV/m$. $E_{inj} = 5\,GeV$.

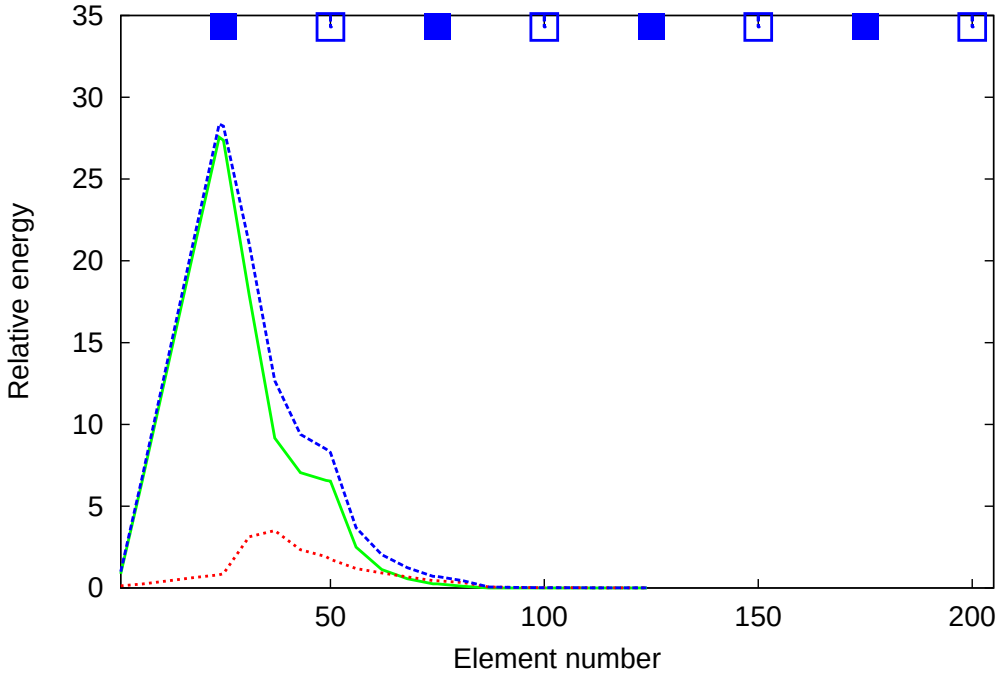

Figure 31: Fowler-Nordheim type emission with $\beta = 150$. Relative energy of primary (solid green), shower secondary (dotted red), and all (dashed blue) particles as a function of the element number. Start in the 9-th FODO cell. $E_{acc} \simeq 24\,MV/m$. $E_{inj} = 5\,GeV$.

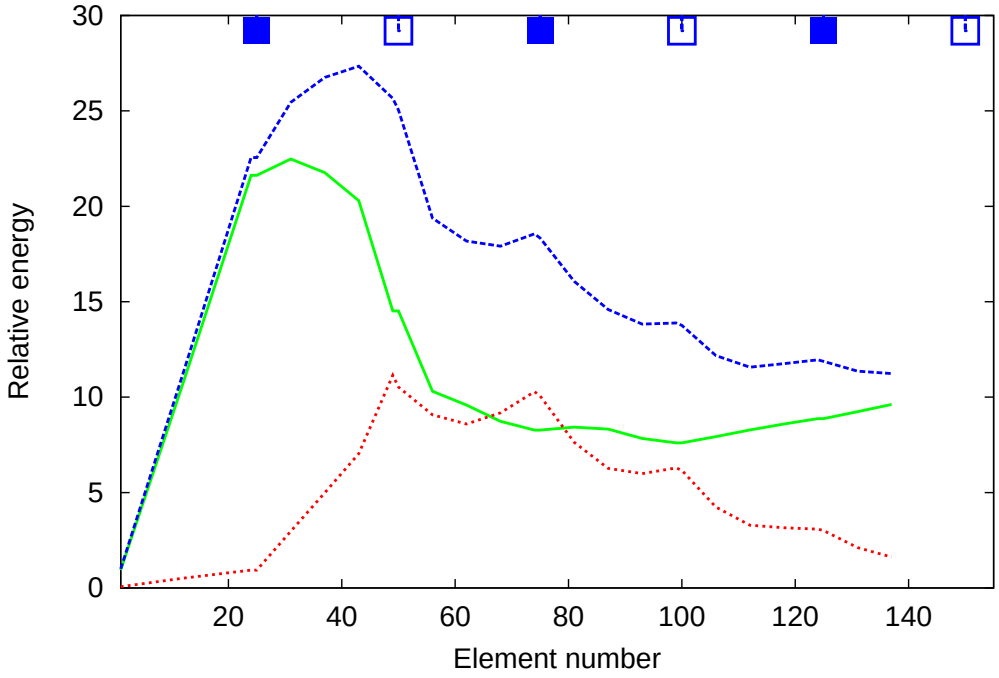

Figure 32: Uniform emission model. Relative energy of primary (solid green), shower secondary (dotted red), and all (dashed blue) particles as a function of the element number. Start in the first FODO cell. $E_{acc} \simeq 100\,MV/m$. $E_{inj} = 5\,GeV$.

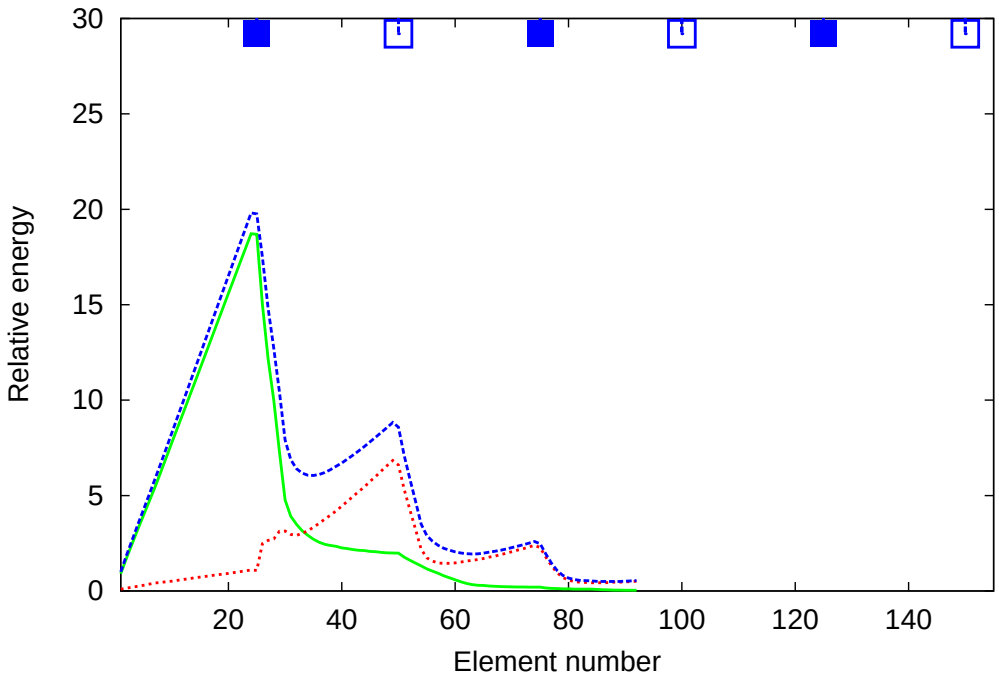

Figure 33: Uniform emission model. Relative energy of primary (solid green), shower secondary (dotted red), and all (dashed blue) particles as a function of the element number. Start in the 9-th FODO cell. $E_{acc} \simeq 100\,MV/m$. $E_{inj} = 5\,GeV$.

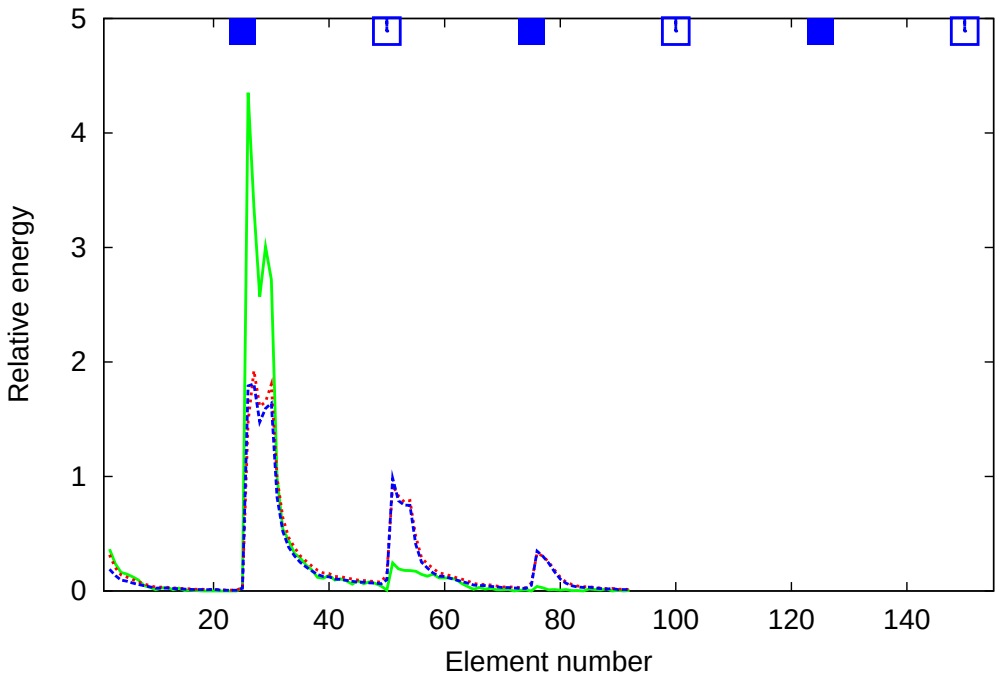

Figure 34: Uniform emission model. Primary impact (solid green), deposited in the element (dotted red), and transmitted transversely (dashed blue) energies as functions of the element number. Start in the 9-th FODO cell. $E_{acc} \simeq 100\,MV/m$. $E_{inj} = 5\,GeV$.

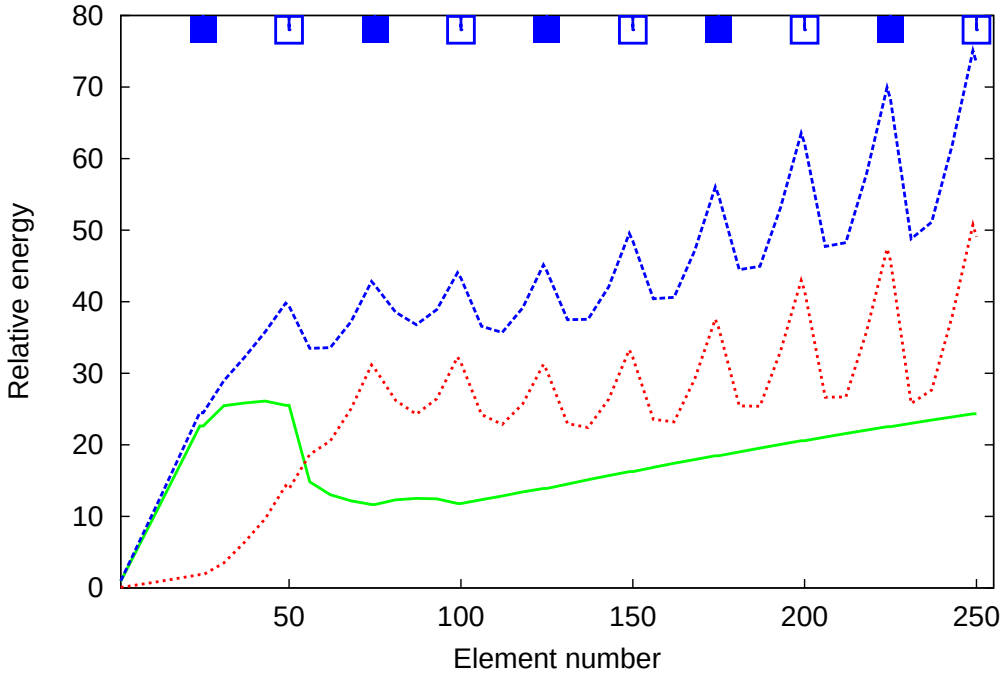

Figure 35: Uniform emission model. Relative energy of primary (solid green), shower secondary (dotted red), and all (dashed blue) particles as a function of the element number. Start in the first FODO cell. $E_{acc} \simeq 150\,MV/m$. $E_{inj} = 5\,GeV$.

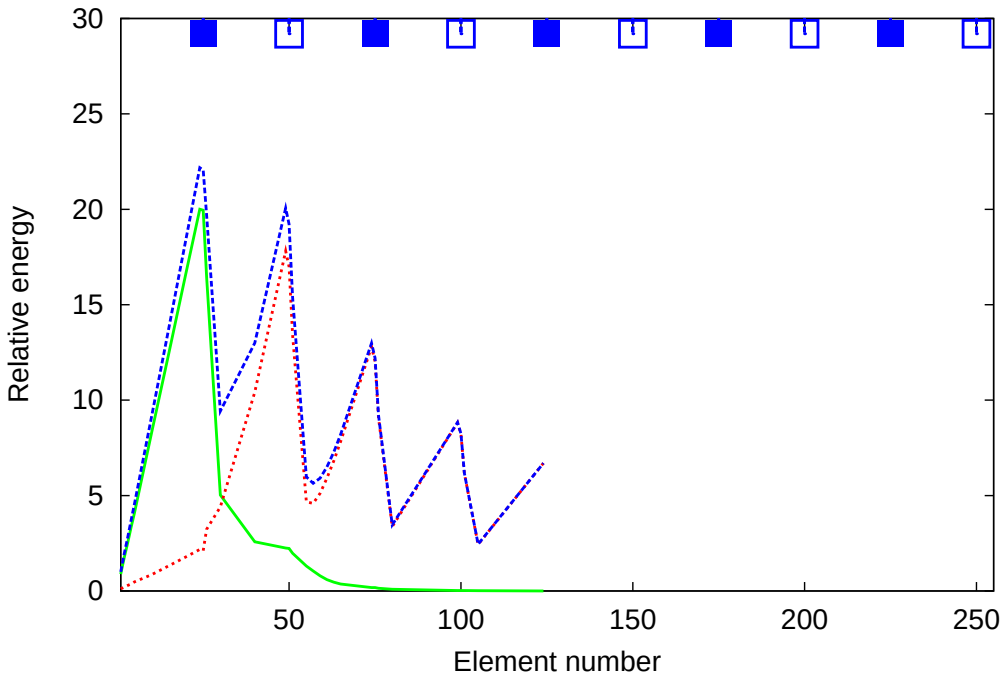

Figure 36: Uniform emission model. Relative energy of primary (solid green), shower secondary (dotted red), and all (dashed blue) particles as a function of the element number. Start in the 9-th FODO cell. $E_{acc} \simeq 150\,MV/m$. $E_{inj} = 5\,GeV$.

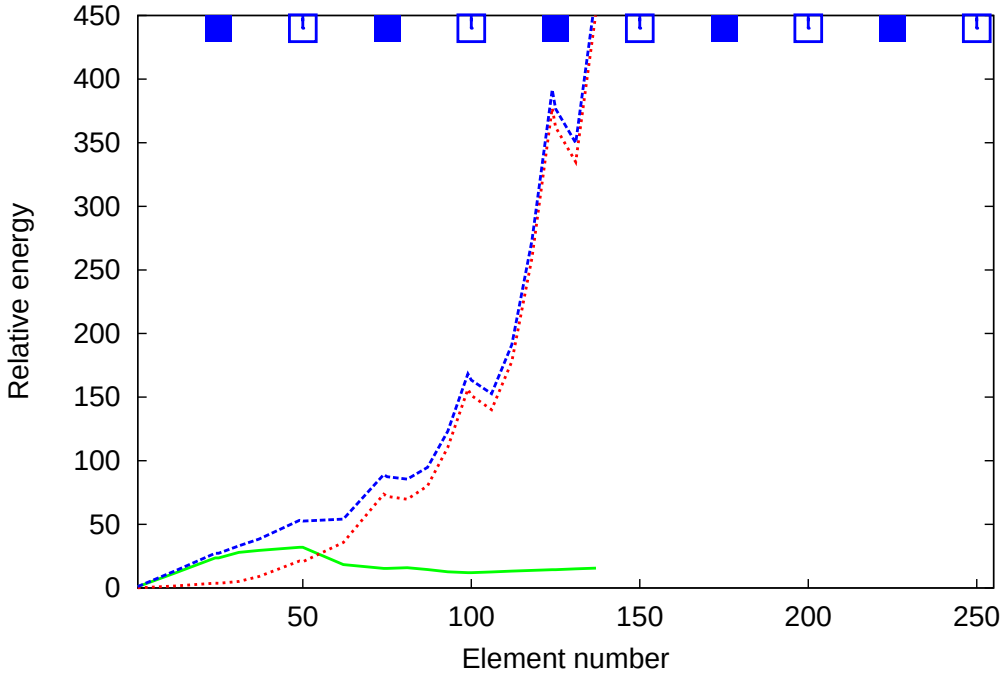

Figure 37: Uniform emission model. Relative energy of primary (solid green), shower secondary (dotted red), and all (dashed blue) particles as a function of the element number. Start in the first FODO cell. $E_{acc} \simeq 200\,MV/m$. $E_{inj} = 5\,GeV$.

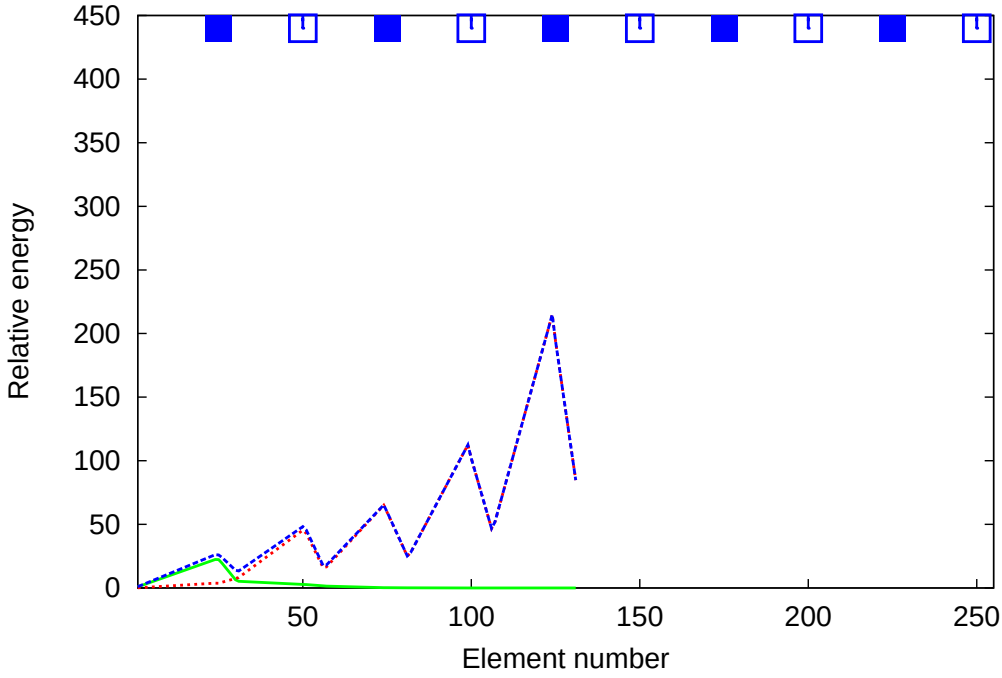

Figure 38: Uniform emission model. Relative energy of primary (solid green), shower secondary (dotted red), and all (dashed blue) particles as a function of the element number. Start in the 9-th FODO cell. $E_{acc} \simeq 200\,MV/m$. $E_{inj} = 5\,GeV$.

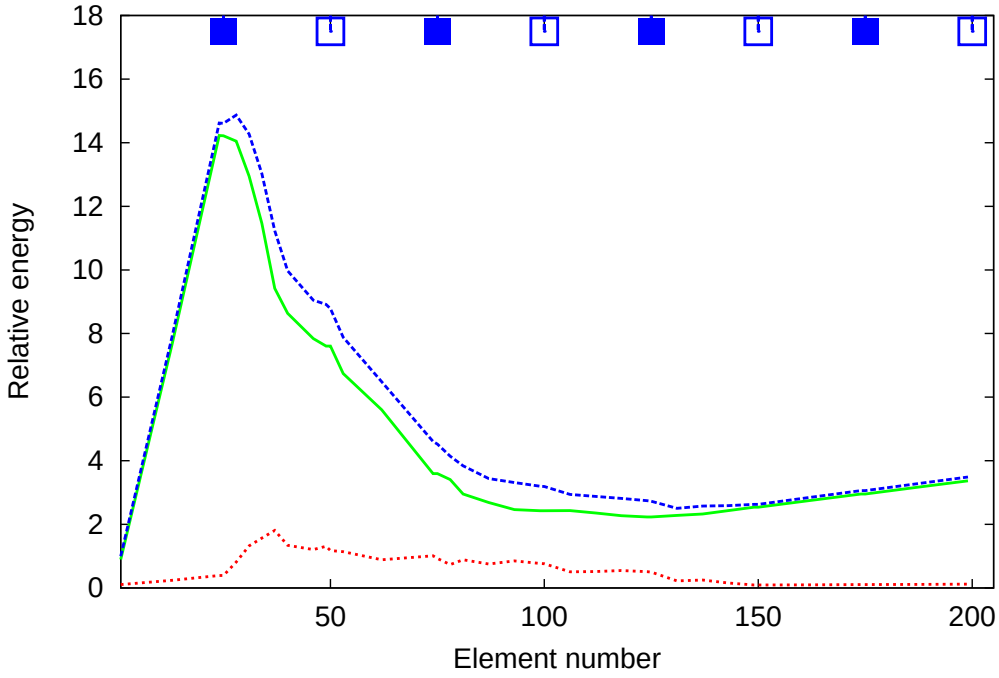

Figure 39: Uniform emission model. Relative energy of primary (solid green), shower secondary (dotted red), and all (dashed blue) particles as a function of the element number. Start in the first FODO cell. $E_{acc} \simeq 24\,MV/m$. $E_{inj} = 3\,GeV$.

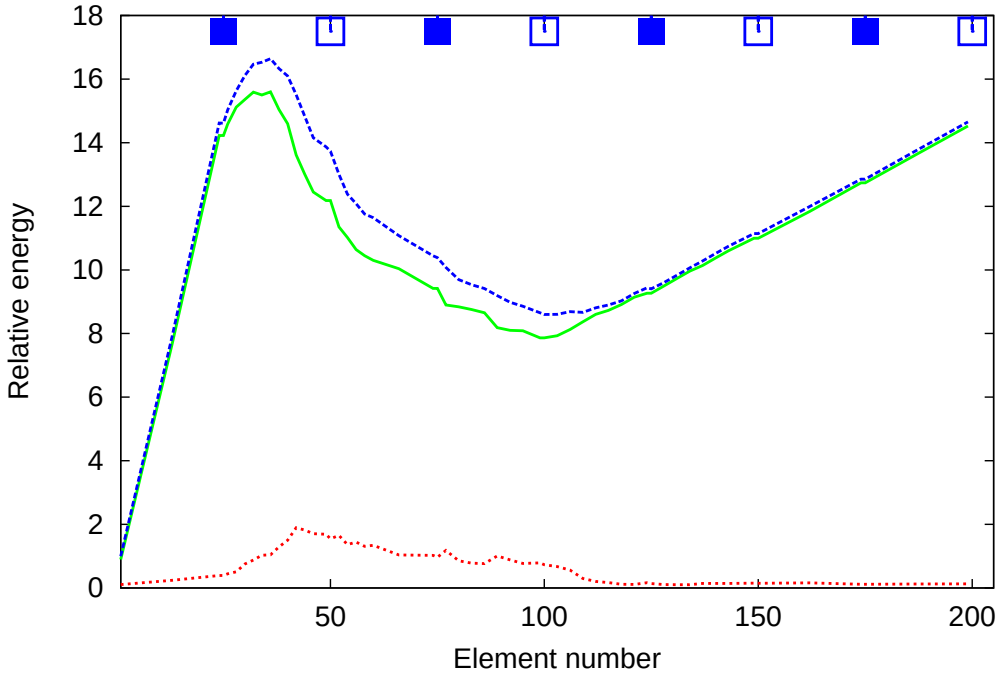

Figure 40: Uniform emission model. Relative energy of primary (solid green), shower secondary (dotted red), and all (dashed blue) particles as a function of the element number. Start in the first FODO cell. $E_{acc} \simeq 24\,MV/m$. $E_{inj} = 1.5\,GeV$.

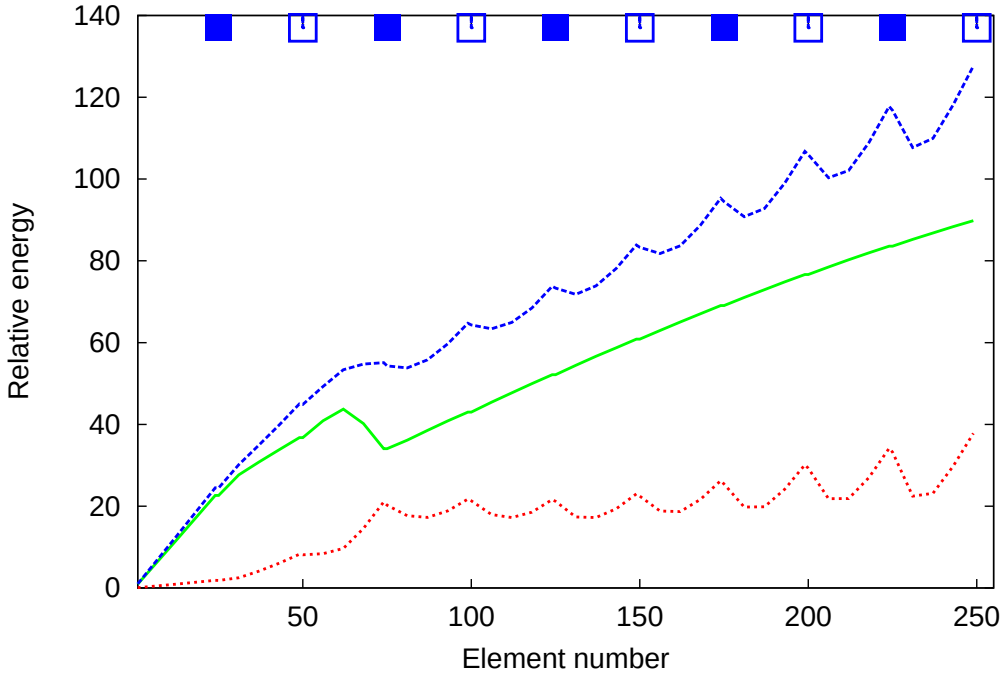

Figure 41: Uniform emission model. Relative energy of primary (solid green), shower secondary (dotted red), and all (dashed blue) particles as a function of the element number. Start in the first FODO cell. $E_{acc} \simeq 150\,MV/m$. $E_{inj} = 1.5\,GeV$.

References

[1] R. Brinkmann, K. Flöttmann, J. Rossbach, P. Schmüser, N. Walker, and H. Weise (eds.), *TESLA Technical Design Report, Part II The Accelerator*, DESY 2001-011.

[2] J.W. Wang and G.A.Loew, *Field Emission and RF Breakdown in High-Gradient Room-Temperature Linac Structures*, SLAC-PUB-7684, 1997.

[3] T.P. Wangler, *Principles of RF Linear Accelerators*, JOHN WILEY & SONS, INC., 1998.

[4] H. Schwettman, J. Turneaure, and R, Waites, *Evidence for surface-state-enhanced field emission in rf superconducting cavities*, J. of. Appl. Phys., **45**, No. 2, 914 (1974).

[5] D. Proch, *Quest for High Gradients*, in: *CERN Accelerator School, Superconductivity in Particle Accelerators*, pp. 201-220, CERN 96-03, May 1996.

[6] B. Bonin, *Field Emission in RF Cavities*, in: *CERN Accelerator School, Superconductivity in Particle Accelerators*, pp. 221-230, CERN 96-03, May 1996.

[7] H. Matsumoto, *Dark Currents*, KEK Preprint 96-120 (1996).

[8] R.J. Noer, *Electron field emission: the past 20 years*, KEK Report 2000-15 (2001).

[9] E. Somersalo, P. Ylä-Olijala, D. Proch, and J. Sarvas, *Computational methods for analyzing electron multipacting in RF structures*, Part. Accel., **59**, 107 (1998).

[10] G. Devanz, *Multipactor simulations in superconducting cavities and power couplers*, Phys. Rev. E, **4**, 012001 (2001).

[11] C. Lyneis, H. Schwettman, and J. Turneaure, *Elimination of electron multipacting in superconducting structures for electron accelerators*, Appl. Phys. Lett., Vol. **31**, No 8, 541 (1977).

[12] L. Kravchuk, G. Romanov, and S. Tarasov, *Multipactoring code for 3D accelerating structures*, Linac 2000, Monterey, vol.2, pp. 821-823.

[13] G. Bienvenu, P. Fernandes, and R. Parodi, *An investigation on the field emitted electrons in travelling wave accelerating structures*, NIM A, **320**, pp. 1-8, (1992).

[14] I. Ben-Zvi, J.F. Crawford, and J.P. Turneaure, *Electron multiplication in cavities*, IEEE Trans. Nucl. Sci., pp. 54-58, (1973).

[15] S. Yamaguchi, *Simulation Studies on High-Gradient Experiments*, LAL/RT 92-18, (1992).

[16] U. Becker, M. Dehler, T. Weiland, *Simulating Dark Current Effects in Linear Collider Structures*, in: *AIP Conference Proceedings 297*, pp. 477-484, CAP 93, Pleasanton, USA, 1993.

[17] B.C. Yunn and R.M. Sundelin, *Field Emitted Electron Trajectories for the CEBAF Cavity*, CEBAF PR-93-025 (1993).

[18] C. Stolzenburg, *Investigation on the development of dark current in superconducting accelerating structures*, Dissertation, Hamburg 1996, 117pp (in German).

[19] N. Akasaka, *Dark Current Simulation in High Gradient Accelerating Structure*, KEK Preprint 96-65 (1996).

[20] H. Grote and F.C. Iselin, *The MAD Program (Methodical Accelerator Design), Version 8.19*, CERN/SL/90-13 (AP).

[21] M.J. Berger, *Monte Carlo Calculation of the Penetration and Diffusion of Fast Charged Particles*, in: *Methods in Computational Physics*, Volume 1, pp. 135-215, Academic Press, New York, 1963.

[22] P.K. MacKeown, *Stochastic simulation in physics*, Springer, 1997.

[23] W.R. Nelson, H. Hirayama, and D.W.O. Rogers, *The EGS4 Code System*, SLAC Report 265 (1985).

[24] E. Hairer, S.P. Norsett, and G. Wanner, *Solving Ordinary Differential Equations I, Nonstiff Problems*, Springer, Berlin, 1987.

[25] E. Hairer and G. Wanner, *Solving Ordinary Differential Equations II, Stiff and Differential-Algebraic Problems*, Springer, Berlin, 1991.

[26] J.M. Sanz-Serna and M.P. Calvo, *Numerical Hamiltonian Problems*, CHAPMAN and HALL, 1994.

[27] J.E. Marsden, *Lectures on mechanics*, Cambridge University Press, 1992.

[28] C.B. Duke, *Tunneling in Solids*, ACADEMIC PRESS, New York and London, 1969.

[29] R.E. Burgess, H. Kroemer, and J.M. Houston, *Corrected Values of Fowler-Nordheim Field Emission Functions $v(y)$ and $s(y)$*, Phys. Rev., Vol. 90, No 4, p. 515, 1953.

[30] J.W. Gadzuk and E.W. Plummer, *Field Emission Energy Distribution (FEED)*, Rev. of Modern Phys., Vol. 45, No 3, pp. 487-548, 1973.

[31] E.L. Murphy and R.H. Good, Jr., *Thermionic Emission, Field Emission, and the Transition Region*, Phys. Rev., Vol. 102, No 6, pp. 1464-1473, 1956.

[32] B. Bonin, *Field Emission and surface conditioning*, Vacuum, Vol. 46, No 8-10, pp. 907-912, 1995.

[33] M. Jimenez, R.J. Noer, G. Jouve, and B. Bonin, *Electron field emission from large-area cathodes: evidence for the projection model*, J. Phys. D: Appl. Phys. **27**, pp. 1038-1045, (1994).

[34] H. Padamsee, K. Green, W. Jost, and B. Wright, *A Statistical Model for Field Emission in Superconducting Cavities*, PAC93 Conference Proceeding, Washington, D.C., USA, pp. 998-1000, 1993.

[35] R.D. Young, *Theoretical Total-Energy Distribution of Field-Emitted Electrons*, Phys. Rev., Vol. 113, No 1, pp. 110-114, 1959.

[36] R.D. Young and E.W. Müller, *Experimental Measurement of the Total-Energy Distribution of Field-Emitted Electrons*, Phys. Rev., Vol. 113, No 1, pp. 115-120, 1959.

[37] J. Sekutowicz, *2D FEM code with third order approximation for RF cavity computation*,

[38] R. Brinkmann, N. Walker, G. Blair, *The TESLA Post-linac Collimation System*, DESY TESLA-01-12, 2001.